**Proudman
Oceanographic Laboratory**

NATURAL ENVIRONMENT RESEARCH COUNCIL

Comparison of finite difference and element models of internal tides on the Malin-Hebrides shelf.

P. Hall [*], A.M. Davies

Proudman Oceanographic Laboratory, 6 Brownlow Street, Liverpool L3 5DA, UK.

Abstract

A three–dimensional baroclinic finite element model with a coarse and fine (i.e. local refinement along the shelf edge) grid is used to examine the influence of shelf edge grid refinement upon the internal tide generation and propagation off the west coast of Scotland. Comparisons are made with observations in the region and with a published solution using a finite difference model. The calculations show that provided that the finite element grid is refined in the internal tide generation area and the adjacent region through which the internal tide propagates, then a numerically accurate solution is obtained. In the regions of strong internal tide generation with a local grid refinement, internal wave energy can accumulate at small scales and must be removed by a scale–selective filter.

1. INTRODUCTION

To date, the majority of intercomparisons between uniform grid finite difference models and unstructured grid finite element models have concentrated upon the barotropic tide. Such a detailed intercomparison was performed by a number of groups in connection with tides in the English Channel, giving rise to a range of papers as part of the tidal flow forum (e.g. Werner 1995; Lynch et al. 1995; Walters and Werner 1989; Walters 1987). In the case of the barotropic tide, it has a long wavelength, and hence little short–scale spatial variability, except in nearshore regions. For this reason an increase in finite element resolution, or map transformation (Johns et al. 1981) combined with boundary–fitted coordinates in a finite difference model to improve coastal resolution is a logical way to refine the grid. Since these early applications of finite element models to barotropic tides, the range of oceanographic problems has increased (see the review of Walters (2005)).

In recent years with increased interest in shelf edge processes (Huthnance 1995) and baroclinic motion, the topic of internal tides has received increasing attention. In the shelf edge region where stratification intersects the shelf slope the motion of the barotropic tide at a frequency x gives rise to an internal tide at the same frequency with non–linear effects giving higher harmonics (Lamb, 2004) and a tidal residual (Xing and Davies 2001a). Internal wave beams at a frequency ω have a slope r given by

$$r^2 = (\omega^2 - f^2)/(N^2 - \omega^2),$$

with N a constant buoyancy frequency and f the Coriolis frequency. Depending upon the relative steepness of topography $s=\nabla h$, with h water depth, the topography is classed as supercritical ($s>r$), critical ($s=r$) or subcritical ($s<r$). Once generated the internal tide propagates away from its generation region along beams. Both on–shelf and off–shelf propagation can occur depending upon the local topography and stratification, with the internal tide being reflected at both sea surface and sea bed. The wavelength of the internal tide varies significantly depending upon local topography variations and stratification, but is typically the order of kilometres rather than the hundreds of kilometres associated with the barotropic tide. For this reason and to resolve the shelf slope, a significantly finer grid is required in the shelf edge region for an accurate representation of the baroclinic tide than that used for the barotropic tide.

Early models of the internal tide were semi–analytical, or used a cross–sectional model (e.g. Craig 1987; Sherwin and Taylor 1990; New 1988; Xing and Davies 1997b) and

---

[*] Corresponding author.

Email address: phh@pol.ac.uk (P. Hall).

hence grid resolution was not critical, in that high resolution could be included everywhere. However, as shown by Xing and Davies (1997b) in a comparison of the numerical solution with the analytical solution of Craig (1987), an across shelf resolution of 3 km with 50 sigma levels in the vertical was required. The reason for this high resolution was that internal tides have a short wavelength. Also their generation at the shelf edge is critically dependent upon shelf slope and vertical stratification. The limitations of using an across shelf "slice" model are well known (Xing and Davies 1998; Legg 2004a,b) in regions where there is an appreciable along shelf forcing such as the area considered here. Consequently, it is essential in such regions to use a full three–dimensional model that can accurately resolve both the across and along shelf variations in topography and density field in the shelf edge region. Consequently, besides refining the grid in the nearshore area in order to reproduce the barotropic tide, it is essential to include an enhanced grid refinement in the shelf edge region. Once generated at the shelf edge the internal tide can propagate both offshelf into the ocean, and onto the shelf. The wavelength associated with this propagation is significantly shorter than the barotropic wavelength. As shown by Hall and Davies (2005) (hereafter referred to as HD05) the short wavelength of internal waves must be taken into account in determining the rate of grid refinement from a fine grid in the region of internal wave generation to coarse grid outside this region. Also, as shown by HD05 in the case of wind–forced internal waves, if the grid refinement is too rapid, small–scale waves are excited and numerical instability can occur. However, by using a Smagorinsky (1963) form of horizontal viscosity, this can be overcome (HD05). The scale–selective filtering associated with the Smagorinsky (1963) form of viscosity is now well known and has been successfully used in Large Eddy Simulation (LES) calculations. This problem is briefly considered here for the case of an internal tide.

The computational requirement in a three–dimensional internal tide model to have a fine grid in the shelf edge region, yet allow for accurate propagation away from this region, is an important consideration in designing an irregular grid. In this paper we examine the problem of internal tide generation off the west coast of Scotland using two unstructured grid resolutions and the QUODDY code. The QUODDY code uses a finite element method in the horizontal and a sigma coordinate approach in the vertical. The vertical eddy viscosity is parameterized using a Mellor-Yamada turbulence model (see later Discussion). As the code and the method used are well established [e.g. see Lynch and Naimie (1993); Ip and Lynch (1995)], details will not be repeated here.

In order to compare results with an existing three–dimensional internal tide finite difference model (Xing and Davies 1998) (hereafter referred to as XD98), the region off the west coast of Scotland was examined. This area is ideal for a model intercomparison study in that there is a strong barotropic tidal forcing in the region, which pro-

duces a significant internal tide. Also the shelf slope is not constant, but the gradient changes appreciably along the shelf edge. This change in gradient and the existence of two off–shelf seamounts which influence the internal tide (XD98) makes the region ideal for the use of an irregular grid. In the calculations performed here, the bottom topography and open boundary forcing were identical to those used by XD98 in a uniform finite difference grid model. By using the same topography and forcing in all calculations, the influence of grid resolution and solution method (namely, finite difference (XD98) or finite element (QUODDY)) upon the solution can be assessed. The main focus of this paper is a model intercomparison study rather than an examination of the processes influencing the generation and propagation of the internal tide, which are covered in detail in XD98. The interested reader is referred to XD98 for details of stratification, energy flux and the role of seamounts and shelf slope in terms of internal tide physics. In the next section (Sect. 2) we briefly describe the topography of the region (with reference to XD98 for detail) and the two irregular horizontal grids used in the calculation. The solution using the finite element sigma coordinate model is described in Sects. 3 and 4. In the final section, results from the inter–comparison of the different grid resolutions and the solution of XD98 are summarized.

2. The hydrodynamic equations, topography of the region, and choice of grid.

The fundamental hydrodynamic equations, which are solved with the various modelling approaches described here, are identical to those solved by XD98. As they are discussed in detail in Xing and Davies (2001b) they will not be repeated here, except to give a general overview of their basic form.

The models are based upon the three–dimensional free surface, nonlinear primitive equations expressed in polar coordinates. The hydrostatic approximation is used, and density is derived from temperature using a simple equation of state (XD98). The models are prognostic in that the temperature field evolves with time due to advection and diffusion terms. Consequently, the on–/off–shelf propagation of the barotropic tide gives rise to internal pressure gradients at the shelf edge and hence an internal tide as described in XD98. Vertical mixing of momentum and density are parameterized using vertical eddy viscosity and diffusivity coefficients which are determined using a turbulence energy closure sub–model (e.g. Blumberg and Mellor 1987; Luyten et al. 1996, 2002; XD98). The coefficient of horizontal viscosity was parameterized using a Smagorinsky (1963) formulation with the arbitrary scaling coefficient taken as C=0.28 (HD05) in the majority of calculations. In a final calculation to examine its influence this value was doubled. The benefits of using this formulation for horizontal viscosity in an internal wave problem involving an irregular grid have been demonstrated in HD05.

Since the calculation, as in XD98, is concerned with the short–term dynamics of the internal tide, rather than its seasonal variation, there is no applied surface heat flux or wind stress. Similarly for the turbulence energy model, there is no turbulence flux through the sea surface or sea bed. A quadratic friction law as in XD98 was applied at the sea bed. Along the open boundary the barotropic tide was identical to that used by XD98. A sigma coordinate was used in the vertical with 40 levels having enhanced resolution in the near bed and near surface region where the internal tide is largest. This is consistent with the vertical resolution used in XD98. In all calculations the model started from a state of rest with zero elevation displacement. In the baroclinic calculation the same temperature profile and hence N^2 profile taken as the strongly stratified case (XD98, see their Fig. 4) was applied everywhere. By this means, in the initial conditions the isotherms were horizontal. In response to open boundary barotropic tidal forcing, in the stratified case a baroclinic tide was generated at the shelf edge. After about six tidal cycles, the influence of the initial conditions was removed and a sinusoidal condition was reached which could be harmonically analysed. In order to separate the internal tide from the barotropic tide, in the baroclinic calculations a barotropic tidal solution was subtracted from the total. This is consistent with the approach adopted in XD98.

The shelf and shelf edge region (Fig. 1) covered by the various models is identical to that used by XD98. The region is characterized by a range of water depths from 2000 m in the deep ocean to the order of 10 m in the near coastal region. At the shelf edge taken as the 200 m contour (Fig. 1), water depths increase rapidly from typically 100 m (on shelf) to 1000 m (oceanic). The movement of the density surfaces over this steep topography, as the tide flows on– and off–shelf, generates the internal tide in this region. To properly account for this generation process and subsequent internal tide propagation, it is essential to resolve topography in this area. To examine the extent to which the internal tide is influenced by grid resolution, calculations were performed with both coarse (2894 nodes) (Fig. 2) and fine (3981 nodes) (Fig. 3) unstructured grids. In the fine grid calculations the grid in the shelf edge region (Fig. 3) was refined in the regions of steeper topography (Fig. 1) in order to accurately resolve the shelf edge slope. This is particularly important, since this together with vertical stratification determines the generation of the internal tide (XD98). Also, as shown by XD98, internal tides are generated in the region of the Anton Dohrn Seamount and Hebrides Terrace Seamount (Fig. 1), and for this reason the grid is refined in these regions (Fig. 3). Ideally, a more gradual change in the mesh size, as the shelf edge is approached than that shown in Fig. 3, would have been preferred. However, this would have increased the computational effort, and as we will show, provided a Smagorinsky form of horizontal diffusion is used, there is no build–up of small–scale waves in the shelf edge region. As the main focus is the baroclinic tide which is dissipated before it reaches the coast, it is tempting to under–resolve the near shore region. However, as the baroclinic tide is forced by the barotropic tide which is significantly influenced by coastal effects, it is necessary to ensure adequate coastal resolution to enable an accurate distribution of the barotropic tidal forcing to be obtained.

3. Tidal distributions computed with QUODDY.

In all calculations the model was started from a state of rest with a constant density in the barotropic case, and horizontal temperature surfaces in the baroclinic calculation. The vertical temperature profile and buoyancy frequency correspond to the strongly stratified case in XD98 (see Fig. 4 in XD98 for details). Motion was induced by tidal forcing across the open boundary, and a periodic state was obtained after 6 tidal cycles, which was harmonically analyzed to give tidal amplitude and phase.

3.1. *Barotropic calculation*

In an initial calculation using the coarser mesh (Calc 1, Table 1) the sea was taken as homogeneous and the three–dimensional barotropic tide was computed. To enable a "like with like" comparison to be performed with XD98, this mesh was generated from the finite difference depth values used in XD98. The cotidal chart (not shown) was not significantly different to that determined by XD98, and showed a northward propagation of the barotropic tide, with tidal amplitude increasing in the coastal region. The observed amphidromic point in the North Channel was reproduced in the model.

A detailed comparison with observations at 41 positions (Table 2, since the location of these gauges is given in XD98 (see Fig. 1a in XD98 for details) it will not be repeated here), showed a similar good agreement with that found by XD98 at offshore locations. However, at coastal positions the accuracy was slightly reduced due to the coarser nature of the unstructured grid in the coastal region than the finite difference grid of XD98 (although the coastline itself is more highly resolved). This is reflected in the slightly higher RMS amplitude error compared to XD98. Obviously, the unstructured grid used here could be refined in the coastal region, but since the main emphasis is on internal tides this was not done.

The computed M_2 surface tidal current ellipse distribution (Fig. 4a) exhibits the same large–scale features found in XD98; in particular, the strong tidal currents in the North Channel and off the west coast of Scotland. The change in alignment of the tidal current ellipses in the shelf edge region from essentially west-east at about 56°N to north-south at about 58°N (where the orientation of the shelf edge changes) found in XD98 is also reproduced here (Fig. 4a). The significant reduction in tidal currents between ocean and shelf and the local intensification of cur-
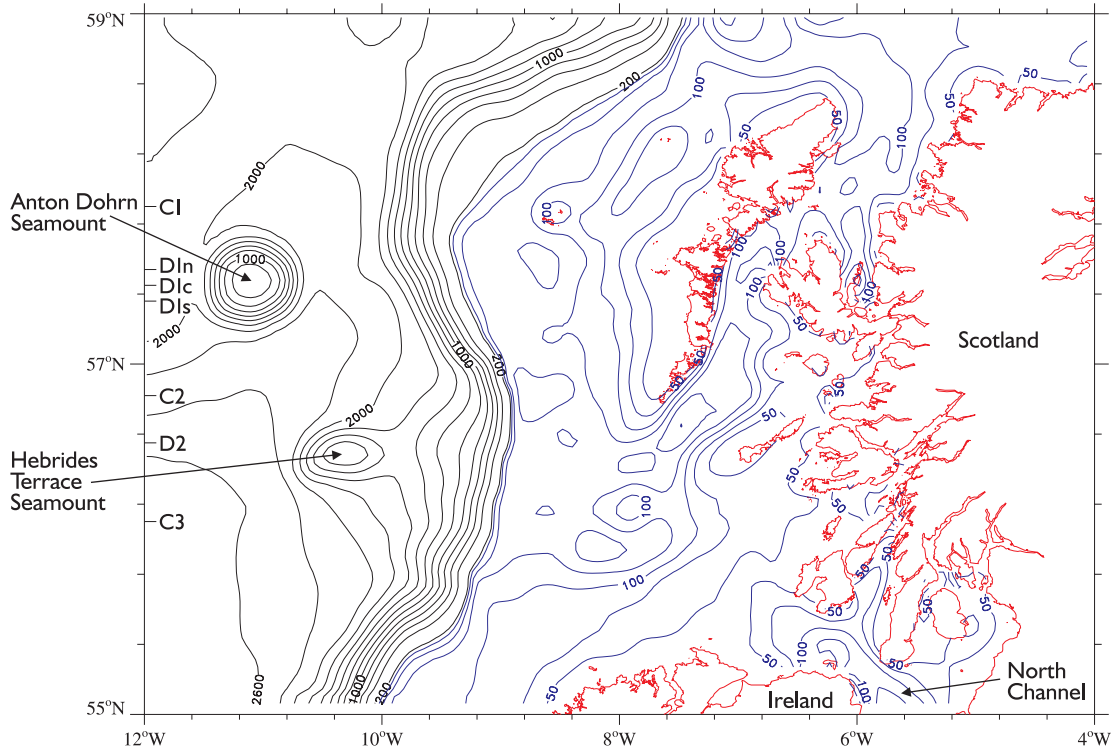
Fig. 1. Bottom topography used in the model. All depths are in metres. The lines marked C1, C2, C3 and D1n, D1c, D1s and D2 denote the latitude of cross–shelf sections used in comparing accuracy of the various grids. Also shown are geographical locations of regions named in the text.

rents over the Anton Dohrn Seamount are shown in Fig. 4a, which was also found by XD98.

A detailed comparison of u and v tidal current amplitudes and phases at a number of offshore observational points (Table 3, since the exact location of these current meters is given in XD98 (see Fig. 1b in XD98 for details) it will not be repeated here) showed similar results to those found in XD98. The water depth h given in Table 3 refers to the total water depth, with sigma (σ) determining the location of the measurement in the water column (namely $\sigma = 0.0$, surface; $\sigma = -1.0$, sea bed). As the main emphasis of the paper is the application of the model to the internal tide, it is useful to examine shelf edge locations (namely T to E, see XD 98, Fig.1b for positions) in more detail in connection with the stratified calculation (see later).

In a subsequent calculation (Calc 2, Table 1) the finer mesh (Fig. 3) was used to compute the barotropic tide. As stated previously to enable a "like with like" comparison to be performed with XD98, this mesh was generated from the finite difference depth values used in XD98. The computed cotidal chart (not shown) was not significantly different to that found using the coarser grid or by XD98. A detailed comparison (not presented) at the locations given in Table 2 where observations are available did not show an appreciable difference between fine grid and coarse grid calculations. This can be readily appreciated, since the finer grid (Fig. 3) is based upon the depths used by XD98, which are

Calc	Resolution (number nodes)	Density
1	2894	Homogeneous
2	3981	Homogeneous
3	2894	Stratified
4	3981	Stratified
5	3981	Stratified (C=0.56)

Table 1
Summary of various calculations.

also used in the coarse resolution grid (Fig. 2). The only difference between the two is a refinement in the mesh in the shelf edge region, and around the offshore seamounts. In practice, if a more detailed bathymetry was available than in XD98, this could be used to enhance the accuracy of the bottom topography as the mesh was refined.

The computed M_2 surface tidal current distribution (Fig. 4b) on the shelf shows a similar pattern to that found with the coarse grid (Fig. 4a). However, in the shelf edge region, the Anton Dohrn Seamount area and Hebrides Terrace seamount, it is clear that with the enhanced resolution in these regions, smaller scale variability than that shown in Fig. 4a can be seen. A detailed comparison of u and v tidal current amplitude and phase at the current observation points (Table 3, Calc 2) showed similar differences to those found with the coarse grid model (Calc 1). At shelf edge locations, H, I, J, K,W and M, N located at about 57°N, both the u and v components of the barotropic velocity are appreciable (of order 15 cm s^{-1}) and are reproduced
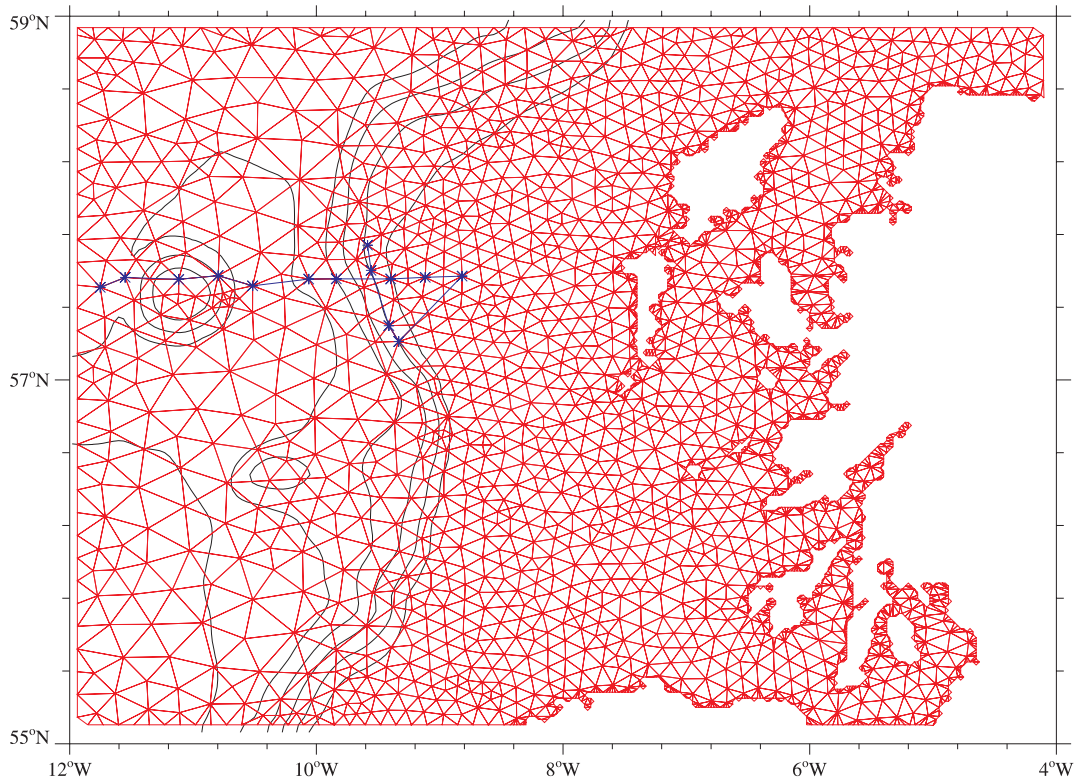
Fig. 2. Coarse irregular Grid (G1) used in the calculations, with location of points used in time series comparisons. (For details of locations, see text).

to a similar level of accuracy on both grids. On average, the tidal current amplitude computed with the finer mesh was larger than the coarse mesh, reflecting its improved ability to resolve the topography. Similarly, further north at locations P, Q, R, S and T, both solutions have similar accuracy and a close correspondence in the distribution of errors with location was found. Since both grids are based on the same distribution of water depths used by XD98 and are adequate for resolving the barotropic tide, then without additional water depth information, there does not appear to be any improvement in accuracy of the finer grid solution compared to the coarser, or the solution of XD98. This is borne out by the RMS errors given in the tables. This result is to a certain extent artificial in that the basic water depths were fixed at those used by XD98 in order to yield a "like with like" comparison. If gridding was performed based on high–resolution depths from a detailed survey of the region (unfortunately not available), then a finer mesh in the shelf edge region with associated improved topography would be expected to improve the results. Improvement of the barotropic tide in coastal regions as the finite element resolution is improved has been found by a number of authors (e.g. Luettich Jr. and Westerink 1995).

3.2. Baroclinic tidal current distribution

In these calculations the stratification corresponded to the strongly stratified case described in XD98 (see Fig. 4 in XD98 for details), and the on–/off–shelf motion of the tide gave rise to an internal tide in addition to the barotropic tide computed previously. The baroclinic tide was separated from the barotropic tide by subtracting the appropriate barotropic tide–only solution.

The computed cotidal chart (not shown) derived with baroclinic effects included using the coarse mesh (Calc 3, Table 1) was not appreciably different to that found under homogeneous conditions. A detailed comparison at observation points showed differences of less than 1 cm and 1 degree, confirming as found by XD98, and in other papers, that tidal elevation was dominated by the barotropic tide.

The surface baroclinic tidal current ellipse distribution (Fig. 5a) shows that the region of strongest generation is at the shelf edge and in the region of the offshore sea–mounts. The internal tide generated at the shelf edge propagates both onshelf and offshelf as described in XD98. The on–shelf propagation of the internal tide is responsible for the appreciable signal to the east of the Hebrides. The presence of stratification influences the vertical eddy viscosity profile and hence in shallower coastal regions it reduces the thickness of the turbulent bottom boundary layer. This in turn influences the barotropic tidal current profile which in
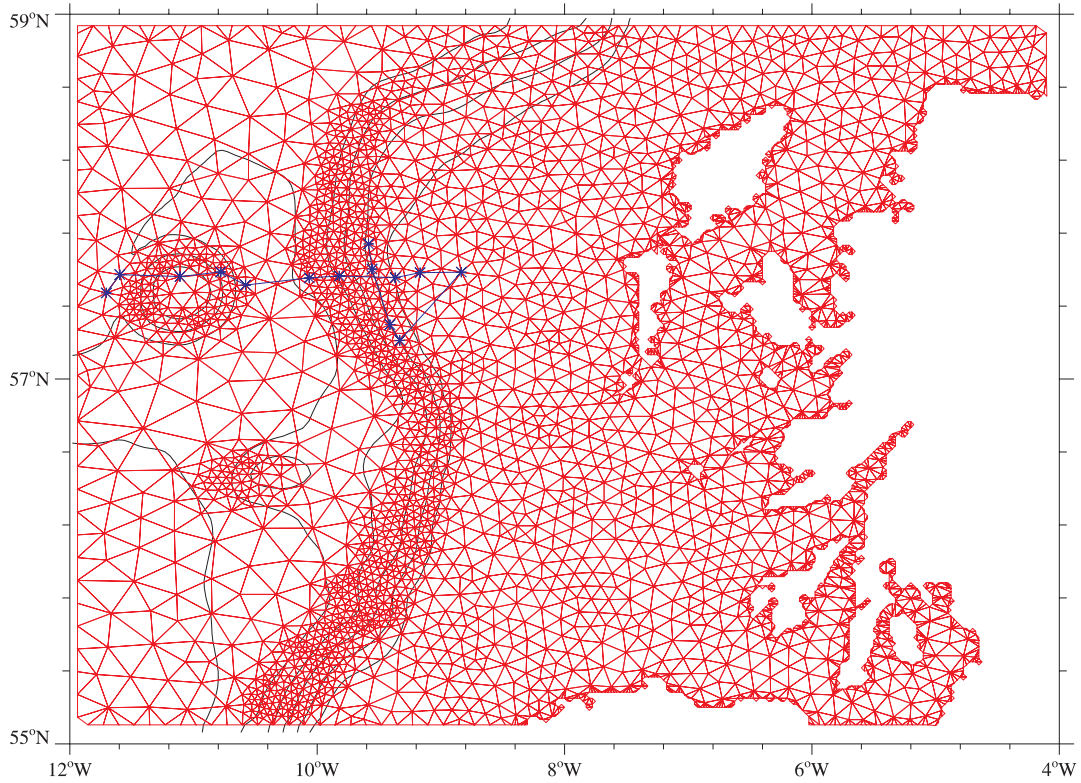
5

Fig. 3. Fine irregular grid (G2) used in the calculations, with location of points used in time series comparisons. (For details of locations, see text).

shallow water is determined by bottom stress and viscous effects. A consequence of this is that the barotropic tidal current computed with the present model is different from that computed without stratification effects. Hence when the two solutions are subtracted a barotropic tidal current remains in nearshore regions. These currents are not due to propagating internal tides but are just due to the difference in bottom stress and internal friction.

A detailed comparison of tidal currents at observational points (Table 3, Calc 3) shows that on the shelf, in the southern part of the region, namely locations A to G, the u and v currents are not substantially influenced by baroclinic effects. However, away from the open boundaries in the shelf edge region, namely locations M, N, W, J, K, H, I (see Fig. 1b in XD98 for locations), the internal tide would be expected to have an effect. Comparison of the u current amplitude on the coarse grid including stratification (Table 3, Calc 3) and the homogeneous solution (Calc 1) shows that the internal tide enhances the vertical variation of current amplitude. A similar effect occurred for the v component of velocity, with its magnitude increasing at a number of locations, see in particular position N, due to the generation of an along slope internal tide. The existence of an along slope internal tide clearly demonstrates the need to use a three–dimensional model, and the limitations of cross slope "slice" models.

Further north at locations, P, Q, R, S and T (see Fig. 1b in XD98 for locations), the u current amplitude is smaller, with the internal tide leading to an increase at some locations (e.g. posn. S). A similar increase occurs in the amplitude of the v current which is the dominant component (e.g. posn. S).

In a subsequent calculation (Calc 4, Table 1), the finer mesh (Fig. 3) was used to determine the baroclinic tide. As previously, the tidal elevation was not significantly affected by the inclusion of stratification. As in Calc (3), the surface tidal current ellipse distribution (Fig. 5b) shows that the internal tide is generated at the shelf edge and in regions of offshelf seamounts. The effect of the enhanced resolution in regions of steep topography is to improve the accuracy of the mesh resolution of bottom topography. Consequently the representation of topographic gradients is enhanced with an associated increase in the detail of the internal tide in these areas (compare Figs. 5a, b). In addition, a more accurate description of bottom topographic gradient influences the degree to which the tide is sub– or super–critical and hence the extent of on–shelf or off–shelf propagation. In particular it is evident from the comparison of Figs. 5a and b that the off–shelf propagation of the internal tide (to the west of the 1000 m contour) that is shown in Fig. 5b was not evident in Fig. 5a due to the lack of resolution in the region. The on–shelf propagation is however evident in both figures. Similarly the enhanced resolution around oceanic topographic features that occurs
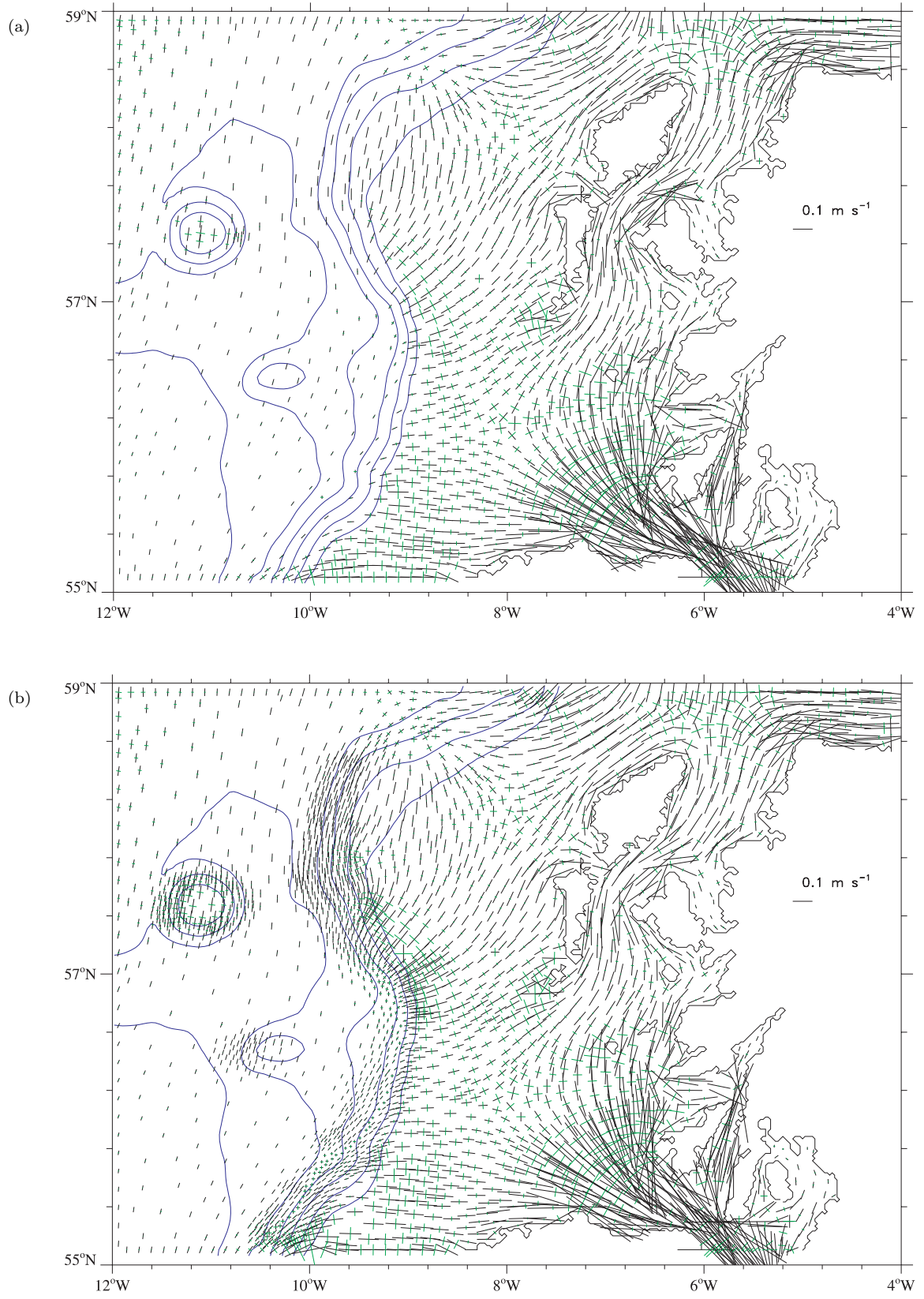
Fig. 4. Computed major and minor axis of the surface M_2 barotropic tidal current ellipse computed a with the coarse grid (Fig. 2), and b the fine grid (Fig. 3).
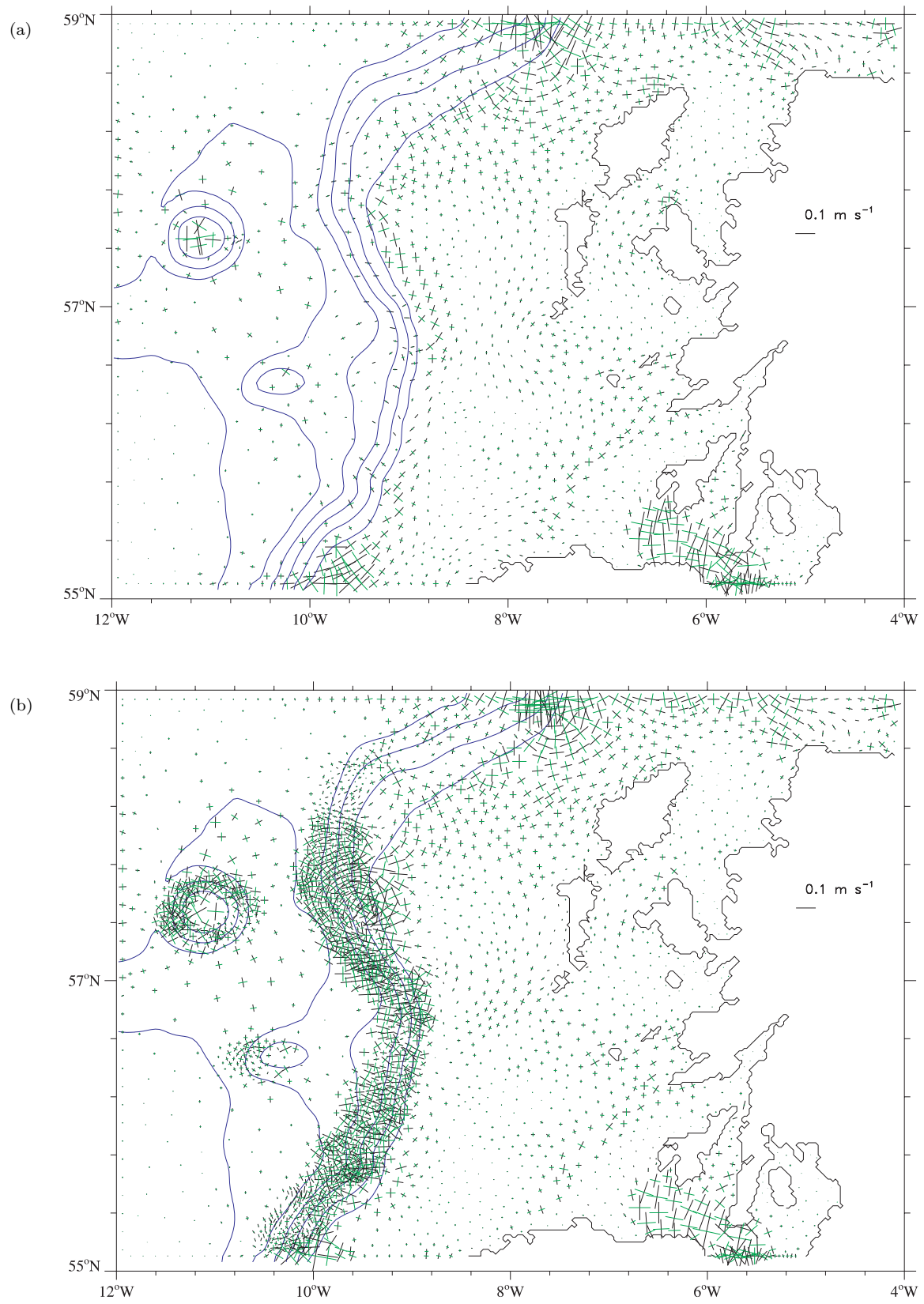
Fig. 5. As for Fig. 4 but for the baroclinic tide.

Posn	Obs		Calc 1	
	h	*g*	*h*	*g*
1.	104	191	96	192
2.	140	208	143	209
3.	119	190	119	191
4.	139	197	131	198
5.	96	175	92	174
6.	106	178	103	178
7.	140	193	133	195
8.	107	176	106	176
9.	129	185	131	185
10.	149	199	148	199
11.	120	177	123	177
12.	153	195	152	195
13.	119	180	129	178
14.	102	169	99	168
15.	101	168	99	167
16.	105	169	102	169
17.	118	171	118	170
18.	156	195	153	195
19.	109	168	108	167
20.	113	232	119	170
21.	118	166	123	162
22.	114	165	123	156
23.	113	163	107	150
24.	65	135	104	150
25.	106	163	104	156
26.	112	163	109	163
27.	101	163	110	153
28.	104	159	102	158
29.	107	157	104	157
30.	57	198	65	187
31.	108	178	112	174
32.	97	175	96	175
33.	16	92	33	126
34.	19	81	40	121
35.	107	342	92	355
36.	116	342	93	354
37.	109	340	92	352
38.	7	125	27	141
39.	43	309	25	281
40.	66	337	63	6
41.	105	340	89	349
RMS error			11.06	15.6

Table 2

Comparison of observed and computed M_2 tidal elevation amplitude h (cm) and phase g (degrees) at a number of coastal and offshore locations, together with RMS errors for Calc 1

in the fine mesh model (Fig. 3) compared with the coarse mesh (Fig. 2) means that finer scale features of the internal tide can be generated in these regions (compare Figs. 5a, b). A detailed comparison of currents at observational points (Calc 4, Table 3) shows that stratification effects appreciably influence both tidal current amplitude and profile, besides its phase in shelf edge regions (compare Calcs 2 and 4 in Table 3). Owing to the absence of a detailed knowledge of the stratification at the time when measurements were made, a rigorous comparison is not possible. In this paper, following XD98, an idealized profile of vertical stratification was used everywhere. As shown by XD98, using a range of density profiles, the spatial distribution of the internal tide and its intensity and energy flux are sensitive to the stratification profile and without a detailed knowledge of this over the whole region, a rigorous comparison with measurements such as those made by Sherwin (1988) is not possible. However, it is evident from a comparison of values in Table 3 (Calcs 3 and 4) that at locations M, N, W, J, K, H, I, the u current amplitude computed on the finer grid is on average larger than on the coarse, with

a slight enhancement in vertical shear. This suggests that the improved cross–shelf resolution in the finer grid has intensified the across–shelf internal tide due to an increased resolution in both its generation and propagation region. In the latter case, an enhanced resolution would be expected to reduce artificial diffusion associated with internal tide propagation (see later Discussion). For the v component which is dominant at locations P, Q, R, S and T, enhanced resolution does not have a major effect. This is to be expected since this component is dominated by along–shelf propagation which, due to its smaller lateral variation, is less sensitive to enhancement in grid resolution.

3.3. *Temporal and spatial variability of the baroclinic internal tide*

In the previous section the influence of grid resolution upon the spatial variability of the surface baroclinic tidal currents was examined in detail. Here we consider how it influences the temporal variability and profile of tidal currents. To this end time series over two tidal cycles of the u and v components of the baroclinic tide both from west to east across the shelf edge, and from south to north along the shelf edge at nodal locations along the lines shown in Figs. 2 and 3 are examined. Time series profiles from both the coarse grid (Fig. 6a, b) and fine grid (Fig. 7a, b) are considered. They are presented in order from west to east, and then from south to north along the lines shown in Figs. 2 and 3.

In deep water (h=1887 m and 1934 m) at the western edge of the model, the u and v profiles of the internal tide computed with either the coarse (Fig. 6a, b) or fine (Fig. 7a, b) grid show similar time variations and profiles, with a slight enhancement in the nearbed region in the coarse compared with fine grid model. In the region of the seamount (h=757 m and 1540 m), particularly at h=1540 m, both the u and v current profile time series computed with the fine mesh model show (Fig. 7a, b) significant variations in the vertical and with time. This appears to be associated with the local production of internal tides in the region of the seamount as discussed in XD98, and will be examined later in connection with cross sections in this region. In the coarse grid model the variation is significantly less (Fig. 6a, b), suggesting that this grid cannot adequately represent internal tide production at the seamount.

At the two deep water positions (h=2171 m and 1912 m) between the seamount and the shelf edge, both grids give weak u baroclinic velocities (Figs. 6a and 7a), although the v component is much stronger and shows a surface intensification and near–surface phase shift. This suggests that in this region the across–shelf component of the internal tide (taken here as the u component) is weaker than the along–shelf component. However, it is evident from the alignment of the topographic contours in the shelf break region (Fig. 5b) that the shelf break changes its orientation in this region giving rise to a significant v component of internal

U velocity grid T2894
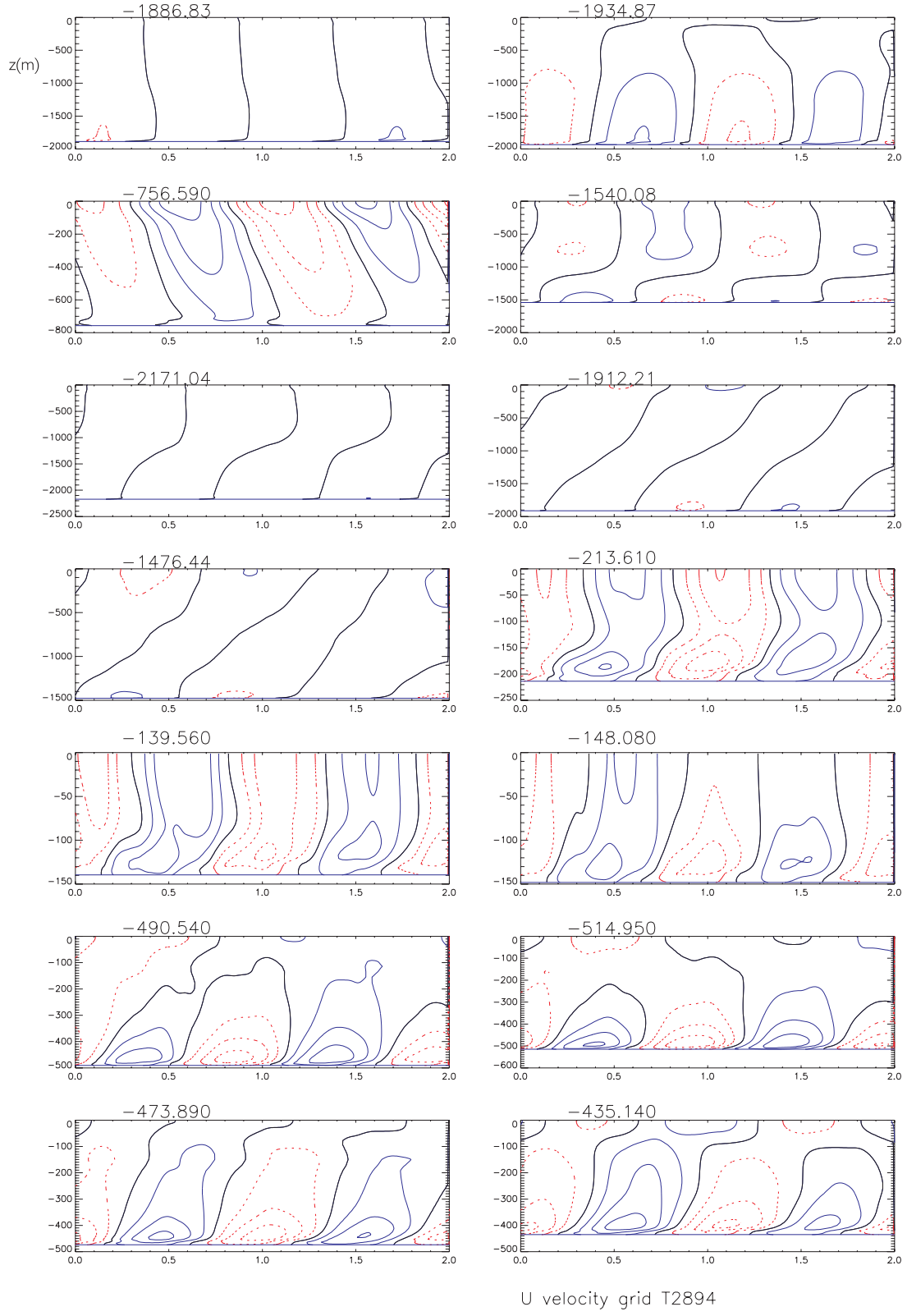
(a)

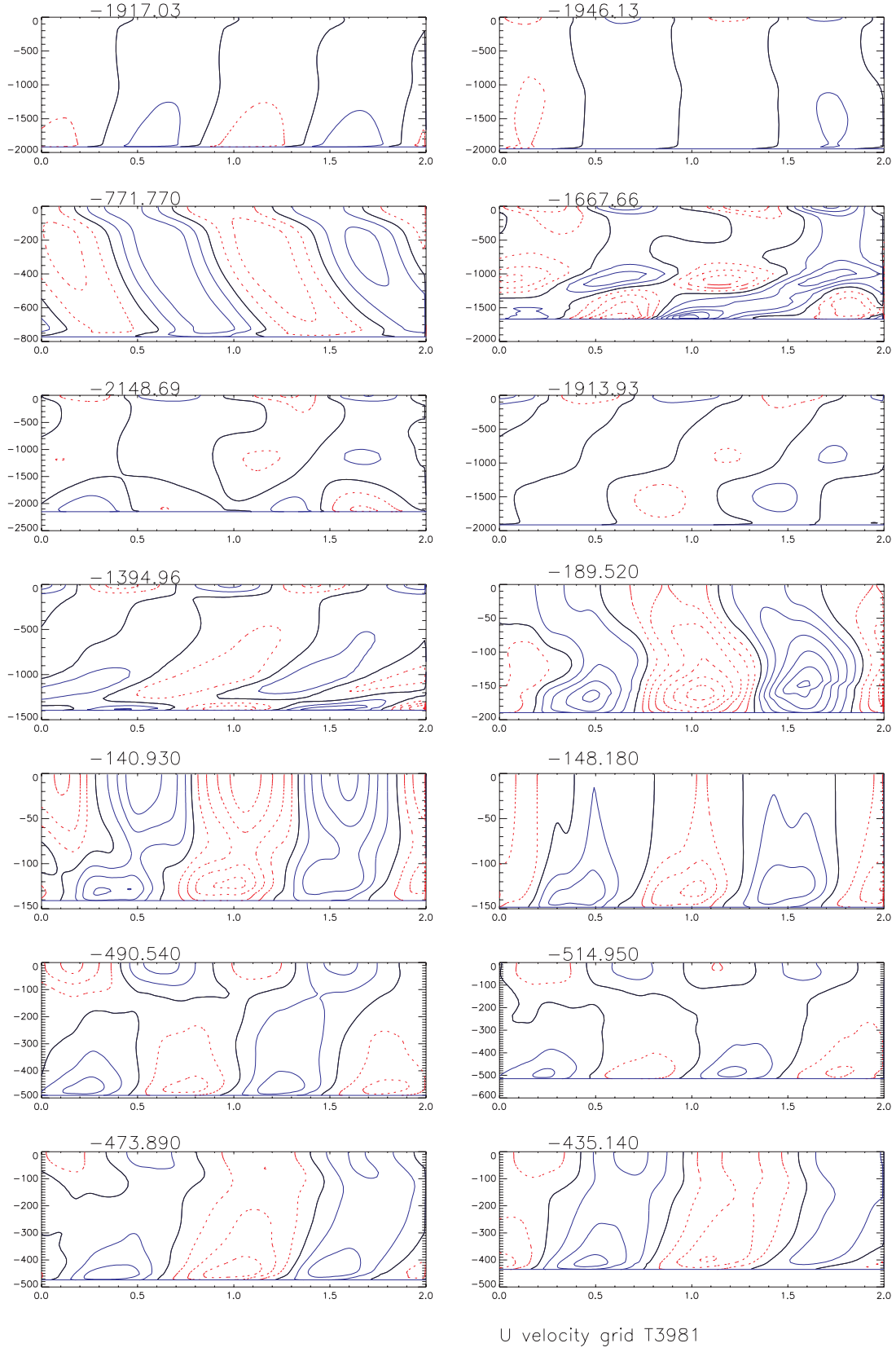Fig. 6. Time series of a u and b v components of the baroclinic tidal current computed with the coarse grid model (Fig. 2) at locations as shown. Contour interval 5 cm s^{-1}, with solid positive, dashed negative (solid black zero).
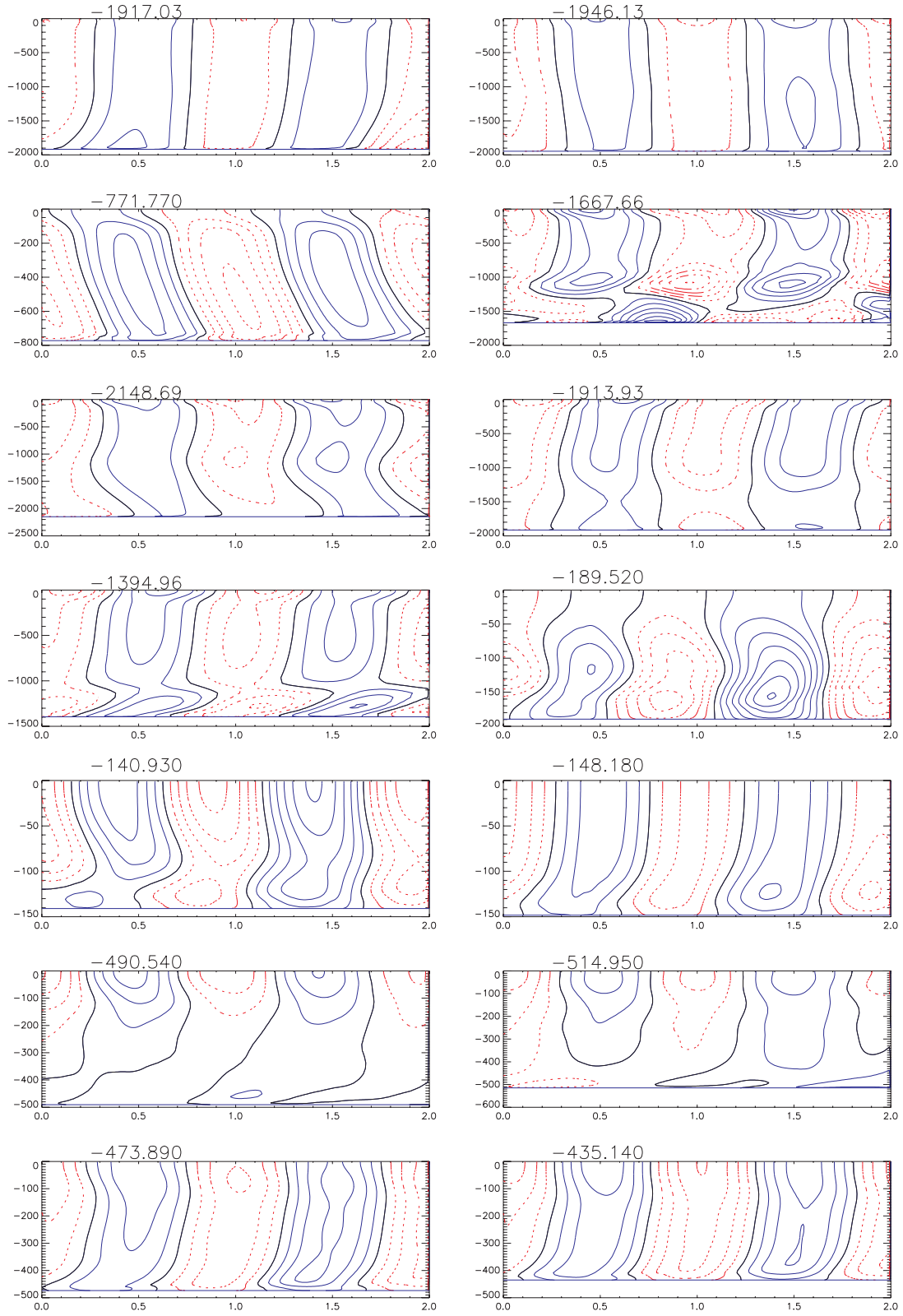
10
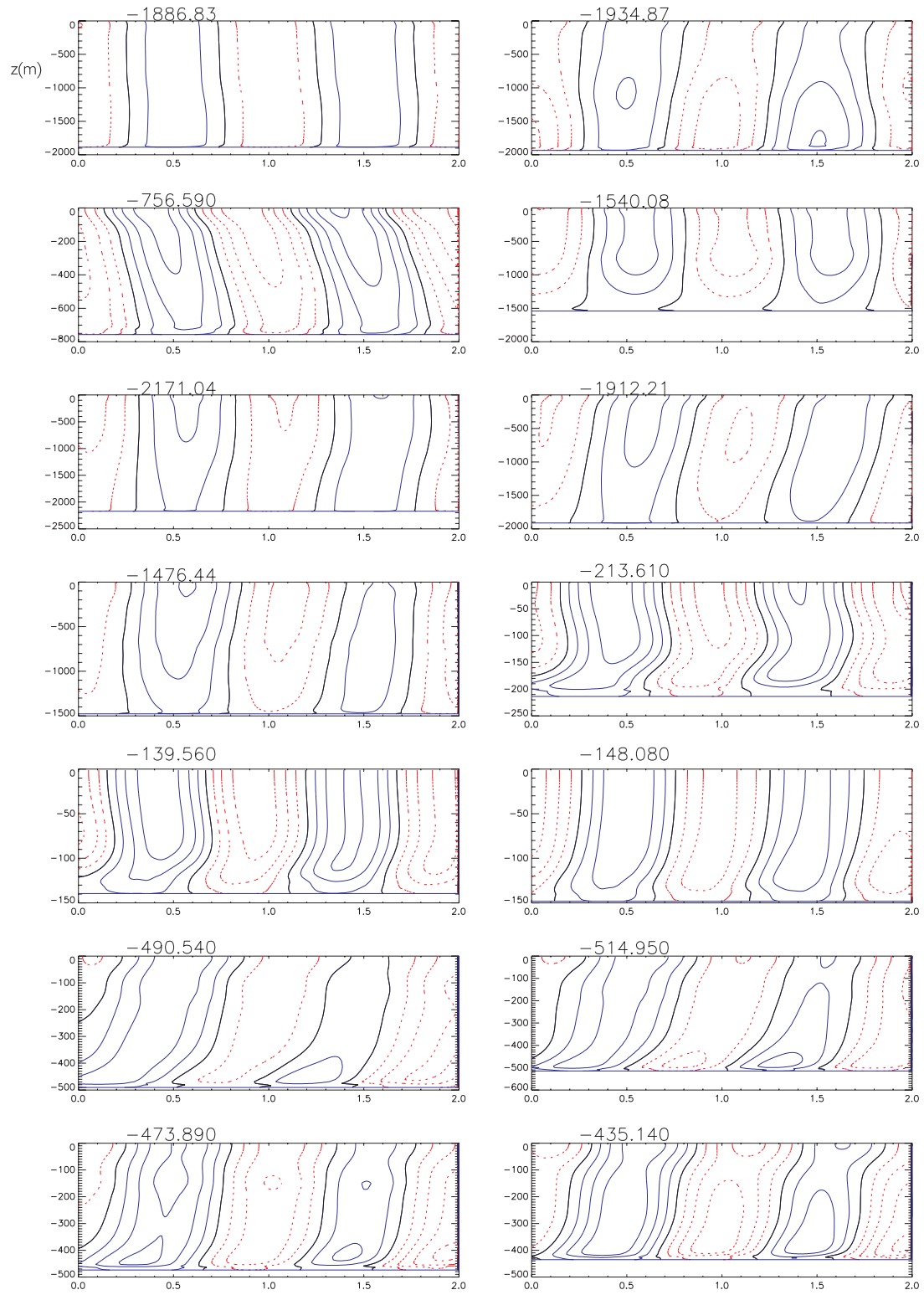
V velocity grid T2894

(b)

Fig. 6. (Contd.)

11

U velocity grid T3981

(a)

Fig. 7. As Fig. 6, but computed with the fine grid model (Fig. 3).

V velocity grid T3981

(b)

Fig. 7. (Contd.)

13

tidal velocity.

On the shelf slope (h=1476 m and 213 m) the u component computed with the coarse grid model rapidly increases from near zero (h=1476 m) to a maximum of >15 cm s^{-1} (h=213 m) as the water shallows (Fig. 6a). For the v component there is an appreciable velocity (of order 15 cm s^{-1}) at both locations, although in the shallower region, current velocities are slightly larger. Both the components of current computed with the finer mesh (Fig. 7a, b) are larger than those determined with the coarse, and show significantly more vertical structure and phase change in the vertical. This suggests that in the shelf slope region there are multiple points at which the internal tide is being generated that can be resolved on the finer mesh but not the coarse. This will be considered later in connection with a detailed examination of the cross shelf variation of the internal tide. On the shelf, at h=140 m and farther to the east (h=148 m), the u and v components computed with both grids show similar current magnitudes and vertical profiles, suggesting that the coarse grid model is sufficiently fine to resolve the on–shelf propagation of the internal tide.

In the case of the along–shelf variation of the internal tide, time series (namely the four locations along the 500 m contour) show a significant change in both the u and v profiles while on going from south to north, reflecting changes in the orientation of the shelf slope and its gradient. The differences between the two solutions appear slightly less at the northern than southern point, reflecting the broader shelf slope and hence smaller gradient. Obviously as the change in topography is reduced, the ability of the coarse grid model to resolve it and hence accuracy of the solution improves.

This comparison of computed time series of the baroclinic tide from ocean to shelf in the region of a seamount and shelf slope shows that a fine grid is required both in the region of internal tide production (shelf slope) and propagation (both onshelf and offshelf) in order to adequately represent the internal tide. In addition in areas of topographic change, namely the seamount and orientation of the shelf slope, the baroclinic tidal velocity is not always dominated by the u component of current.

4. Shelf edge cross–section comparisons

4.1. *Influence of mesh resolution*

To compare results in more detail with those derived using a uniform grid (XD98), and examine the influence upon the internal tide of using two different mesh resolutions in the shelf edge region, contours of the amplitude of the u component of the baroclinic tide along cross sections C1, C2, C3 and D1, D2 (see Fig. 1 for latitude of these lines) were examined. Distributions of u current amplitude across these cross sections were examined in detail in XD98. To be consistent with XD98, we will concentrate upon the upper part of the shelf slope and the adjacent shelf region along

sections C1, C2 and C3. Along D1 and D2 we will examine the seamount and slope. Initially results are presented from the coarse grid solution (Fig. 2).

Contours of u current amplitude at cross section C1 (Fig. 8a), show a minimum at about 11°W at a depth of 1100 m, with amplitude increasing towards the sea surface. This is consistent with XD98, although in this case, there was a local minimum at this depth at about 10.5°W (see XD98, Fig.13a). The rapid increase in amplitude close to the shelf edge, with a local maxima at about 700 m was also found in XD98. A reduction at midwater of tidal current on the shelf, and associated surface regions of enhanced tidal current amplitude is also consistent with XD98. As shown in XD98 (see their Fig. 3c) and in Davies and Kwong (2000), there is an appreciable along– and across–shelf barotropic energy flux in this region, with the potential to generate an internal tide. Besides this, the vertical variation of stratification and gradient of topography is such that the components of the across– and along–shelf internal tidal forcing functions (F_x, F_y) are large in the shelf edge region at cross section C1. A detailed discussion of this together with contours of F_x, F_y are given in XD98 (see their Figs. 3d, e). The large values of F_x, F_y along the shelf slope at cross section C1 explains the strong baroclinic currents along the shelf slope. Internal tidal energy propagates vertically both onshore and offshore from its generation point, being reflected at the sea surface and seabed, leading to regions of intensified current magnitude (Fig. 8a). This is discussed in detail in XD98 where internal tide energy density contours are presented (see Fig. 13b in XD98).

At cross section C2, the region of minimum tidal current that extends from sea surface to a depth of 1500 m at about 10°W is consistent with that found in XD98. Also, the increase in the magnitude to the west and east of this region as the surface is approached was found in XD98. However, an oceanic region (to west of 9°W) of surface–enhanced tidal current amplitude (exceeding 9 cm s^{-1}) shown in XD98 is not present. On the shelf regions of enhanced surface and near bed velocity separated by a minimum are clearly evident, although the intensity and lateral extent of these regions is less than that given in XD98. The reason for this is that the magnitude of the forcing functions F_x, F_y, and the intensity of the energy flux beams depends upon the gradients of topography which are not as well resolved in the coarse grid model as in XD98.

An oceanic surface layer of enhanced current amplitude was not present at cross section C3 (Fig. 8c), although such a region was found by XD98. Although an area of enhanced u surface current amplitude was found above the shelf break, the magnitude of currents in this region and along the shelf edge (Fig. 8c) were below those found by XD98. Again this was related to lack of resolution in the coarse mesh model.

These results suggest that the magnitude of the internal tidal currents particularly in the oceanic region, computed with the coarse grid model, are below those found by XD98. To see to what extent this conclusion is valid in the region

Table 3 — Comparison of observed and computed M_2 tidal current. Columns are grouped under **U component** and **V component**; each group contains σ, observed amplitude/phase (Obs), and four computed solutions (Calc 1–4) with amplitude U_h / V_h (cm s^{-1}) and phase U_g / V_g (degrees).

Posn	Water depth h	U: σ	Obs U_h	Obs U_g	Calc1 U_h	Calc1 U_g	Calc2 U_h	Calc2 U_g	Calc3 U_h	Calc3 U_g	Calc4 U_h	Calc4 U_g	V: σ	Obs V_h	Obs V_g	Calc1 V_h	Calc1 V_g	Calc2 V_h	Calc2 V_g	Calc3 V_h	Calc3 V_g	Calc4 V_h	Calc4 V_g
A	73	-0.44	17.6	170	18.7	161	17.9	158	19.0	168	17.9	159	-0.44	4.7	80	3.4	50	3.1	17	4.0	58	3.5	29
	73	-0.86	14.1	158	16.6	158	15.9	155	11.9	149	14.9	149	-0.86	3.4	357	1.4	26	2.1	334	4.8	297	4.8	325
B	54	-0.44	46.8	202	44.2	189	43.9	191	42.2	191	43.0	192	-0.44	10.1	187	5.4	162	6.7	144	4.4	172	6.3	148
	54	-0.48	45.2	202	43.8	189	43.6	191	41.6	191	42.2	192	-0.48	6.7	183	5.4	163	6.6	146	4.2	178	5.8	151
	54	-0.80	33.6	192	39.0	187	38.7	189	35.6	187	35.9	188	-0.80	10.8	239	5.7	178	6.3	159	4.7	213	4.5	183
C	58	-0.33	82.9	234	74.3	221	72.7	218	73.3	222	71.8	219	-0.33	50.8	77	55.7	64	61.4	62	55.1	66	61.5	63
	58	-0.36	82.2	234	74.0	221	72.4	218	72.7	222	71.2	219	-0.36	56.1	75	55.2	64	61.0	62	54.5	65	60.9	63
	58	-0.81	69.0	233	65.0	220	63.6	217	62.2	221	61.7	218	-0.81	41.4	73	45.5	62	50.6	59	44.6	59	50.4	58
D	110	-0.95	46.9	242	42.5	223	42.4	223	31.1	220	31.2	221	-0.95	31.6	22	31.7	26	31.7	26	39.3	11	39.4	9
E	136	-0.82	13.7	140	9.3	108	8.4	109	10.5	104	12.4	111	-0.82	7.3	63	5.3	18	4.7	15	8.2	12	8.9	25
F	44	-0.75	26.8	91	18.5	93	18.0	92	18.2	92	17.8	92	-0.75	70.3	70	65.0	54	64.1	54	63.6	54	63.6	54
G	170	-0.18	11.2	159	9.1	112	9.8	105	8.4	107	8.8	96	-0.18	8.7	88	9.2	63	8.4	59	7.1	61	6.3	58
	170	-0.71	15.6	116	9.1	107	9.9	100	9.9	118	9.7	111	-0.71	12.2	41	8.6	59	7.8	54	9.5	61	8.9	66
H	126	-0.80	16.5	113	15.6	103	16.7	103	15.9	92	17.7	86	-0.80	11.3	46	9.6	52	10.3	49	8.2	21	8.6	6
I	134	-0.27	25.4	127	14.3	127	18.9	118	11.3	116	14.3	101	-0.27	18.2	53	11.7	79	13.9	68	9.4	65	6.8	20
	134	-0.79	13.9	139	14.3	124	18.7	116	17.0	106	22.6	90	-0.79	14.1	69	11.3	77	13.5	66	10.0	48	13.6	18
J	139	-0.32	24.7	126	19.3	119	22.1	116	16.5	105	14.8	90	-0.32	16.1	54	14.0	61	15.6	66	9.5	36	4.9	19
	139	-0.82	19.9	119	18.5	116	21.2	113	22.9	111	30.4	83	-0.82	13.2	63	12.9	60	14.6	58	13.9	39	18.7	356
K	138	-0.86	18.4	131	14.6	106	15.6	107	21.0	101	18.4	66	-0.86	11.5	56	8.1	59	9.1	63	11.8	29	10.6	343
	138	-0.35	22.9	153	14.6	109	15.7	110	11.6	101	11.3	107	-0.35	16.8	64	8.4	62	9.4	66	8.4	50	6.3	56
W	140	-0.46	19.1	150	19.7	141	22.6	138	24.5	125	22.4	117	-0.46	16.0	82	19.2	81	22.4	77	17.9	52	14.0	51
	140	-0.82	17.5	153	17.6	137	19.8	135	25.0	128	21.8	109	-0.82	14.5	84	16.8	81	19.7	78	18.7	59	10.9	37
L	589	-0.49	5.4	271	8.3	261	10.1	264	18.4	222	21.2	249	-0.49	11.9	188	14.9	177	16.2	182	22.0	144	26.6	167
	589	-0.83	2.2	207	8.5	256	10.3	257	13.9	271	13.8	317	-0.83	8.1	185	15.0	175	16.3	177	19.3	183	20.7	218
	589	-0.92	2.9	196	8.1	251	9.8	252	12.2	286	12.6	338	-0.92	8.0	180	14.5	172	15.6	175	17.8	194	19.0	231
M	1614	-0.13	1.0	30	0.5	13	0.7	270	3.3	348	6.4	87	-0.13	6.9	200	6.8	180	6.3	184	8.7	189	4.2	188
	1614	-0.32	1.7	83	0.5	13	0.7	270	2.3	278	6.1	109	-0.32	5.3	198	6.8	180	6.3	184	10.2	175	5.9	158
	1614	-0.69	1.8	230	0.5	13	0.7	270	1.0	139	11.7	81	-0.69	8.3	180	6.8	180	6.3	184	8.6	171	4.5	141
N	145	-0.38	17.1	161	12.3	166	13.8	183	18.7	155	19.5	141	-0.38	14.8	103	14.0	115	18.1	115	19.8	95	16.8	89
	145	-0.83	11.2	186	10.6	158	11.0	179	18.8	135	23.0	127	-0.83	13.5	151	11.9	116	15.5	117	17.0	79	17.6	70
	145	-0.83	13.9	151	10.6	158	11.0	179	18.8	135	23.0	127	-0.83	11.3	105	11.9	116	15.5	117	17.0	79	17.6	70
O	135	-0.44	5.7	163	7.8	125	6.7	120	7.6	120	6.9	113	-0.44	14.7	159	11.3	141	12.5	147	10.6	145	11.8	150
	135	-0.81	9.5	145	8.1	119	7.3	115	10.9	132	10.0	134	-0.81	11.3	147	10.6	141	11.9	146	12.1	125	14.0	131
P	194	-0.22	11.2	203	4.3	161	4.9	181	3.6	221	3.8	216	-0.22	17.8	168	10.5	181	11.2	170	14.9	185	15.4	190
Q	177	-0.86	8.5	193	5.4	156	5.1	166	12.3	179	11.2	170	-0.86	12.9	172	10.6	177	10.9	173	15.7	145	13.4	152
R	155	-0.35	7.9	232	4.0	156	4.4	153	0.9	245	1.4	295	-0.35	17.1	182	12.5	180	11.9	175	15.4	194	16.3	199
	152	-0.34	9.1	201	4.0	156	4.3	153	0.9	251	1.5	296	-0.34	14.3	171	12.5	180	11.9	175	15.5	194	16.4	199
	155	-0.84	10.3	162	5.2	150	5.4	151	11.4	180	11.6	180	-0.84	8.8	144	11.6	175	11.3	171	16.3	148	15.8	150
S	146	-0.28	5.7	234	4.3	154	4.4	149	0.9	40	1.4	354	-0.28	14.4	192	12.4	183	12.0	182	15.0	202	16.3	205
	142	-0.80	9.2	194	5.4	153	5.5	150	10.7	187	11.2	188	-0.80	12.7	172	11.8	179	11.5	178	17.0	156	17.2	156
	146	-0.83	8.9	188	5.4	152	5.6	149	11.4	186	12.0	186	-0.83	11.2	172	11.7	179	11.4	177	17.1	153	17.3	153
T	142	-0.47	3.7	191	6.9	128	6.9	129	6.8	107	5.10	109	-0.47	14.6	195	12.6	185	12.6	186	12.2	195	13.6	198
	142	-0.82	6.6	178	7.6	129	7.5	131	8.7	167	8.3	180	-0.82	12.8	188	12.3	183	12.3	184	15.9	166	17.2	171
U	110	-0.77	22.0	140	18.3	176	17.2	175	20.7	173	19.0	149	-0.77	8.0	354	8.8	157	7.7	171	9.3	136	1.9	138
V	114	-0.90	17.1	152	14.3	163	14.5	155	16.2	155	16.3	145	-0.90	14.2	237	19.0	244	17.9	248	17.3	251	16.9	255

Table 3: Comparison of observed and computed amplitude U_h (cm s^{-1}) and phase U_g (degrees) of the u component of the M_2 tidal current at a number of depths and locations, and also comparison of data for v component.

of the seamounts a similar comparison was performed along sections D1 and D2 (Fig. 1).

The computed values of the u–current amplitude along a cross section in the region of the Anton Dohrn Seamount showed significant spatial variability, with current amplitude varying from the northern edge of the seamount (cross section D1n), (Fig. 8d) to the centre of the seamount (cross section D1c) (Fig. 8e) and to its southern edge (cross section D1s) (Fig. 8f). At cross section D1n (Fig. 8d) in the region above the seamount, the internal tide was a minimum at about 500 m below the surface. However, its value at this location rapidly increased as the surface was approached, reaching a surface maximum above the seamount in excess of 14 cm s^{-1}. Similarly going from a depth of 500 m down to the top of the seamount, the magnitude of the u velocity amplitude increased (Fig. 8d). The regions of maximum u–amplitude were also evident at depth and along the shelf slope. Small regions of local surface enhancement of u–amplitude are also evident above the shelf break. This suggests that local generation is occurring along the shelf slope and the slope associated with the seamount, with propagation giving rise to regions of surface maximum. This spatial distribution of the internal tide, in particular the minimum at 500 m in the region above the seamount, and the rapid increase above this point as the surface is approached is consistent with the results presented in XD98. However, XD98 found a more rapid increase in u–amplitude on going from z=500 m down to the top of the seamount than that found here. In addition an extensive region of enhanced surface u–current amplitude occurred rather than the limited region shown in Fig. 8d.

To examine to what extent the solution was sensitive to the exact position of the cross–section, Fig. 8e shows contours along a cross section (D1c) slightly to the south of D1n. It is evident from Fig. 8d and e that although moving farther south has only a slight influence upon the distribution of topography, in particular a slight broadening of the top of the seamount, it has an appreciable effect upon the amplitude of the internal tidal current above the seamount. Although just above the seamount there is still a minimum at z=500 m, the amplitude increases rapidly with distance above and below this location. A local maximum at z=700 m occurs just above the seamount as found in XD98. In addition, the region of surface u current amplitude maximum increases compared to Fig. 6d, although its lateral extent is still below that found in XD98.

At cross section D1s, situated at the southern edge of the seamount, its height is appreciably less than at D1c, and there is only a slight increase in u–amplitude above the seamount. However, a local increase along the eastern edge of the seamount and along the continental slope particularly at depth as found at cross section D1c, is evident (Fig. 8f). These changes in internal tidal current magnitude in the region of the seamount can be related to the spatial variations in the forcing functions F$_x$, F$_y$ in the seamount region (see XD98).

These calculations clearly show that in the region of the

Anton Dohrn Seamount, the cross–shelf variation of the internal tide is particularly sensitive to location relative to the peak of the seamount. Although XD98 never examined this sensitivity, they performed calculations with and without the seamount (see Fig. 17 in XD98) and showed the importance of the seamount in determining the distribution of the internal tide in this region. The calculations of forcing functions F$_x$, F$_y$ (see Fig. 3d, e in XD98 for detail) and energy flux vectors (see Fig. 3c in XD98) showed that both across– and along–shelf components of the internal tide were generated in this region. Since the distribution and magnitude of F$_x$, F$_y$ depends on topographic slope, the variations in this slope in the seamount region will influence the internal tide distribution. The differences in the ability of the finite element mesh or finite difference grid to reproduce this slope will influence the distribution of the internal tide in this region. This explains in part the differences in u–amplitude between the present model and those presented in XD98 in the region of this seamount.

Further south at cross section D2 (Fig. 1) corresponding to the Hebrides Terrace Seamount, u–amplitude contours show (Fig. 8g) a surface and sea bed maximum in the region of the seamount. A local maximum along the continental slope also occurs at a depth of 1000 m (Fig. 8g). The location of these maxima is consistent with that given in XD98. As at other cross sections and as found by XD98, surface and bed current maxima occur in the region of the shelf slope.

To examine in detail to what extent the internal tide is influenced by resolution, comparable cross–section plots to those shown in Fig. 8 computed with the finer grid (Fig. 3) are presented in Fig. 9. Considering initially cross section C1. Although refining the grid does not substantially affect the large–scale features of the internal tide distribution (compare Figs. 8a and 9a), it does increase the u–amplitude particularly in the surface layer and along the shelf slope. Considering initially the oceanic (west of 10°W) distribution in Fig. 9a. Although the minimum that occurs at 1000 m is consistent with that found in Fig. 8a, it is evident that amplitude increases more rapidly in Fig. 9a, than Fig. 8a, as the surface is approached. This gives rise to a significant increase in the surface layer over which the amplitude exceeds 5 cm s^{-1} (Fig. 9a) compared to Fig. 8a, and is consistent with XD98. Similarly local surface and bed maxima occur at about 9.5°W, associated with the shelf break region (Fig. 9a), that were not present previously (Fig. 8a). Some indication of these can be found in XD98, although the grid resolution of that model was insufficient to represent them in detail. Regions of local maxima in the near bed region both on the shelf and along the shelf slope that could not be adequately resolved previously (Fig. 8a) are evident in Fig. 9a, with amplitude increased above that found in XD98 due to improved resolution.

A significant increase in amplitude and lateral extent of the region of u surface current in proximity of the shelf break is clearly evident in Fig. 9b compared to Fig. 8b, due to enhanced resolution in the shelf slope and offshelf region
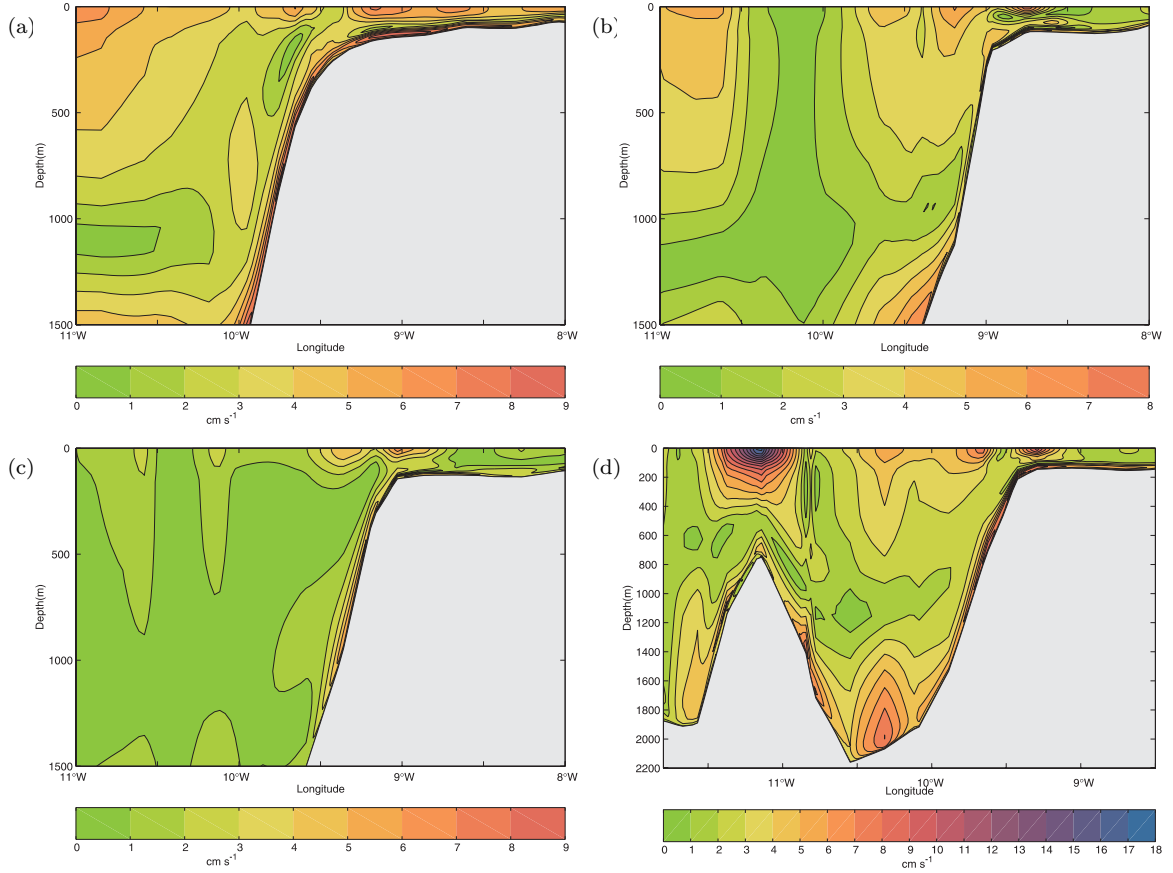
Fig. 8. Contours of the amplitude (cm s^{-1}) of the u component of the baroclinic tidal current at cross sections a C1, b C2, c C3, d D1n, e D1c, f D1s and g D2, computed with the coarse grid (Fig. 2) with C=0.28.

in the fine (Fig. 3) compared to the coarse (Fig. 2) grids. In addition on the shelf in the region adjacent to the shelf break, the magnitude of surface and near bed maxima (Fig. 7b) are increased beyond those found with the coarser grid (Fig. 8b) and given in XD98. Similarly at depth (z=1200 m) along the shelf slope there is a region of local intensification (Fig. 9b) that did not occur previously (Fig. 8b) and although present in XD98, was under–resolved and spread in the horizontal.

A similar increase in the shelf edge and offshelf surface current maxima occurs along cross section C3 in the fine compared with coarse grid calculation (compare Figs. 9c and 8c). However, these values are still below those observed by Sherwin (1988) in this region. This may be due in part to the fact that Sherwins observations were at slightly different locations (of order 50 km away) and this will influence comparisons in regions of high spatial variability. The existence of multiple surface maxima in the shelf edge region is shown in XD98, although their magnitude is less, and their lateral extent larger, suggesting that the internal wave energy that propagates into the ocean in the XD98 calculations may have spread in the horizontal. In theory the internal tide propagates offshore along ray paths which must be resolved on the grid. If lateral resolution in the ocean is coarse (Fig. 2), then these ray paths are not re-

solved and energy is not focused along well–defined beams. With improved resolution (XD98) compared to the coarse grid model (Fig. 2), the ray paths are better represented and regions of surface maxima are resolved, although there can be some lateral spreading. With enhanced resolution (beyond that in XD98) (Fig. 3), ray paths and regions of surface intensification are resolved. In addition, with enhanced horizontal resolution, the shelf slope can be more accurately resolved provided a detailed depth survey is available to match the grid resolution. As shown by Xing and Davies (1999), as smaller scale cross–shelf variations of topography are resolved along the shelf edge, the number of internal tide generation points increases leading to a significantly more complex cross–shelf distribution of the internal tide. In the case of the along–shelf variation of the internal tide, Legg (2004a) showed a local intensification of the nearbed internal tide on the same length scale as the along–shelf corrugations in topography. This suggests that to reproduce these small–scale variations, the mesh size needs to be significantly smaller than the dominant length scale, of the fine scale undulations in topography. Differences in internal tidal current magnitude compared with Sherwin (1988) will also be due to the differences in the density field, suggesting that for a detailed model/data comparison an extensive survey of the density field with sufficient resolution
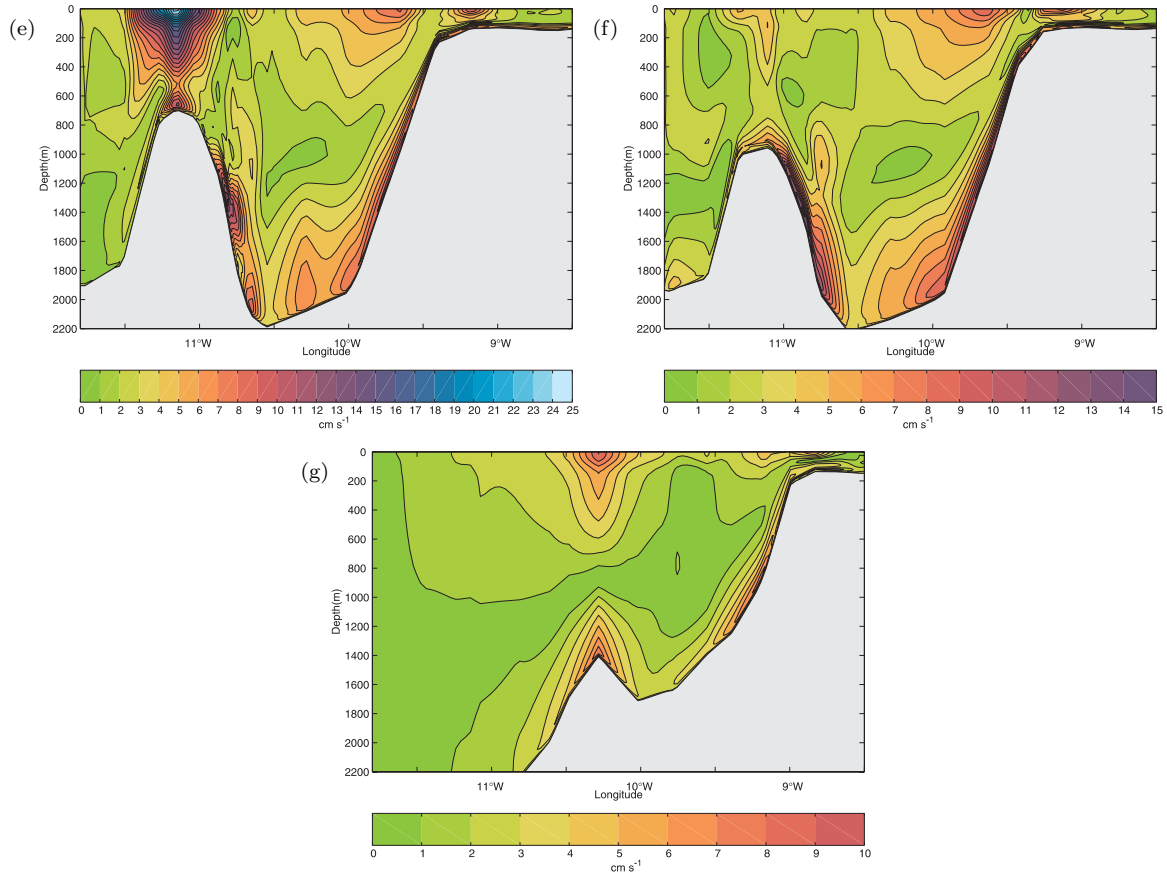
17

Fig. 8. (Contd.)

to match the model grid is required. However, as shown by Xing and Davies (1997c) short–term wind effects can modify the density field and thereby influence the internal tide and its interaction with the wind (Davies and Xing 2003).

The presence of a region of enhanced current amplitude along the shelf slope (Fig. 9c) computed with the finer grid compared to previously (Fig. 8c) further illustrates the benefits of using enhanced resolution in the shelf slope region. This bed enhancement was also found in XD98 with their finite difference grid.

The internal tide at cross section D1n (Fig. 9d) computed with the finer grid shows a significantly larger surface and bed enhancement in current amplitude above the seamount (Fig. 9d) than found previously (Fig. 8d). Also the lateral extent of the region of enhanced u surface current amplitude (Fig. 9d) exceeds that computed with the coarser resolution (Fig. 8d).

Further south at cross section D1c, again above the seamount there are regions of surface and nearbed enhancement of current magnitude separated by a region at about z=500 m where the magnitude is a minimum (Fig. 9e). In addition, surface current magnitude in the region between the shelf break and the surface maximum above the seamount is enhanced above that found in the coarser grid solution (Fig. 8e). The magnitude of the maximum currents in this surface layer exceed those given in XD98,

where the region of maximum surface currents was spread over a larger area. The region of rapid spatial variability in amplitude contours on the eastern side of the seamount was not found in XD98 probably due to lack of resolution in this area.

Contours of current amplitude in the near bed region both along the eastern side of the seamount and in the shelf slope region show significant small–scale variability, suggesting that these boundary layers cannot be adequately resolved. The inability of the model to resolve these boundary layers gives rise to a Gibbs type effect and an increase in energy on a length scale comparable to the mesh size in the model. This effect was found by HD05 in the wind–forced internal wave field on an irregular grid, and could only be removed by increasing the coefficient (C) in the Smagorinsky formulation of horizontal momentum diffusion. The effect of changing this coefficient is examined in the next section.

Contours of tidal current amplitude at cross section D1s show (Fig. 9f) similar large–scale features to those along D1c, (Fig. 9e). However, significantly smaller scale (of the order of the grid scale) oscillations of a nonphysical nature are present. As with cross section D1c, the influence of the Smagorinsky coefficient C upon these will be examined in the next section.

The effect of refining the grid in the region of cross section D2 is to increase the amplitude above the seamount in
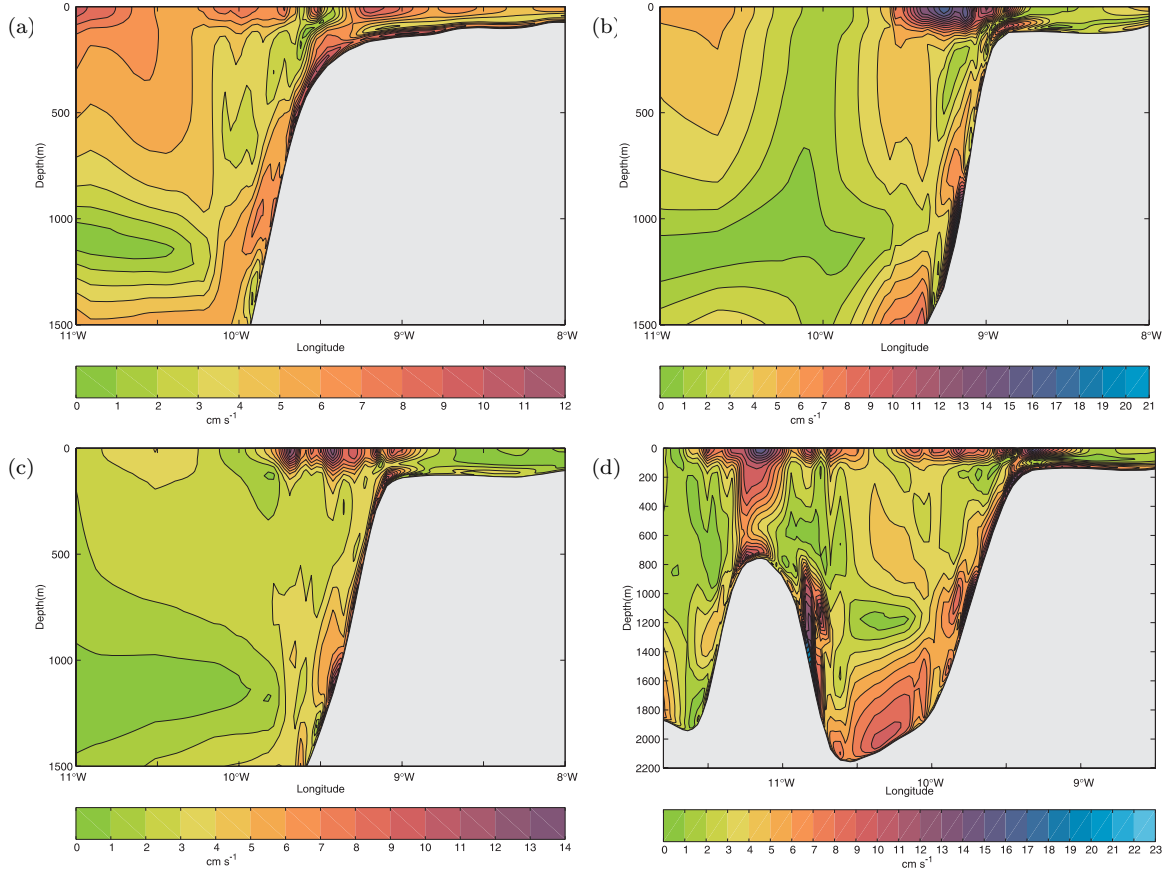
18

Fig. 9. As Fig. 8, but for the fine grid (Fig. 3) with C=0.28.

the nearbed region (Fig. 9g) compared to the coarser grid solution (Fig. 8g). The corresponding maximum at the surface does, however, show small–scale variability (Fig. 9g) compared to that found previously (Fig. 8g). The surface maximum above the shelf break, and the local maximum at a depth z=1000 m along the shelf slope (Fig. 9g) are significantly larger than found previously (Fig. 8g) or in XD98, reflecting the improved resolution in the present calculation. The influence of increasing C upon the current distribution along cross section D2 will be examined in the next section.

4.2. *Influence of coefficient C upon baroclinic tidal current distribution*

In this calculation (Calc 5, Table 1) the fine grid distribution was used, although the coefficient C in the Smagorinsky formulation of horizontal viscosity was doubled from its previous value to C=0.56. Along cross section C1 the effect of increasing C had little effect upon the distribution of tidal current amplitude contours (not shown), except for a slight reduction in maximum values in the near bed region along the shelf slope. At this cross section the tidal current shows a fairly smooth change (Fig. 9a) from ocean to shelf that appears to be well resolved. At cross section C2, away from the shelf break and shelf slope a fairly smooth varia-

tion of tidal current amplitude occurs which is not significantly influenced by the increase in C (compare Figs. 10a and 9b). However, at the shelf break and particularly along the shelf slope at z=1200 m, there are some rapid small–scale changes on the grid scale of the model in the tidal current amplitude above the bottom boundary layer (Fig. 9b). These appear to be physically unrealistic in that there are no small–scale variations in bottom topography in this region. Also they appear just above the bottom boundary layer and suggest a Gibbs type numerical problem in fitting a relatively smooth current profile to a high sheared bottom boundary layer. If they are physically realistic, and due to wave trapping or reflection they are of such a small scale that they cannot be accurately resolved on the present grid and need to be removed by a scale–selective filter, before they destabilize the solution (see HD05 for more details of the numerical problem). The effect of increasing C is to remove these ripples giving rise to a smoother and resolvable distribution (compare Fig. 9b and Fig.10a). A similar effect of increasing C was found along cross section C3, (not shown) where small–scale inadequately resolved variations along the shelf slope were removed.

In the region of the Anton Dohrn Seamount, considered here in terms of cross sections D1c and D1s, the effect of increasing C is to reduce the small–scale variations along the eastern side of the seamount and the shelf slope (com-
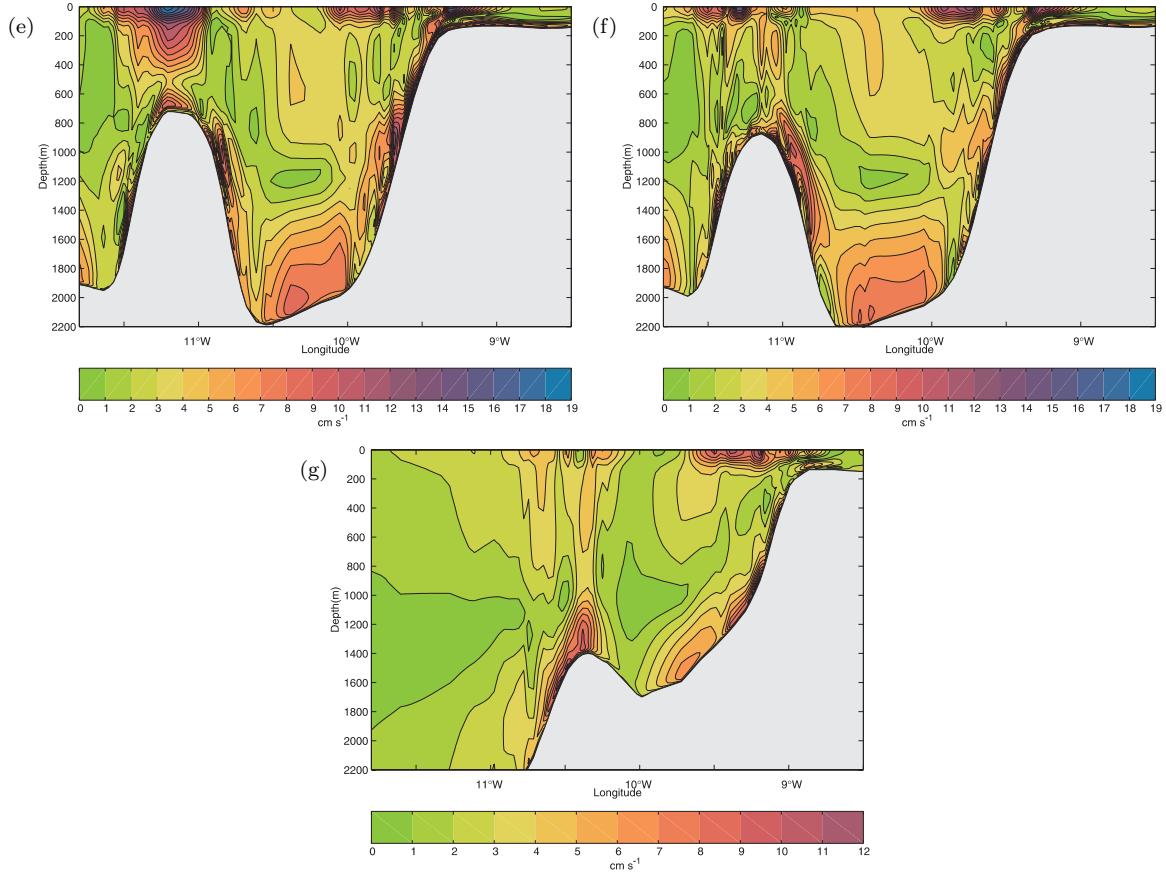
Fig. 9. (Contd.)

pare Fig. 9e, f with Fig. 10b, c). Although increasing C in this case does reduce the small ripples, leaving the large–scale features essentially unchanged, it is evident from Fig. 10b, c that some small–scale spatial variability does remain. This may be realistic in that as shown by Xing and Davies 1997a, 1999, small–scale topographic features along shelf slopes give rise to the local regions of internal tide generation. In this case a further grid refinement to that shown in Fig. 3 is required to increase the accuracy of the solution in these regions.

In a final comparison, cross section D2 was examined. As previously the increase in C removed small–scale features particularly along the shelf slope region (compare Fig. 10d and 9g) without affecting the large–scale pattern. Obviously to improve the accuracy of the solution in the region of rapid changes in shelf slope, a finer horizontal grid would be required.

5. Concluding remarks

The QUODDY finite element code with both a coarse and fine grid (in which the grid was refined in the shelf slope region) has been used to compute the three–dimensional baroclinic tide in the Malin-Hebrides shelf edge region off the west coast of Scotland. This region was chosen because it has a significant internal tide and was the area of a recent measurement study. In addition the internal tide besides being generated along the shelf slope is also produced along the slope associated with two offshelf seamounts. These additional sources of the internal tide, plus spatial variations in the orientation and slope of the shelf edge provide a good test of a variable resolution grid model. A detailed solution is also available from a regular grid finite difference model of the region (XD98) with which irregular grid solutions can be compared.

Initial calculations showed that for the three–dimensional barotropic tide there were no substantial differences between the coarse or fine grid solutions and that of XD98. This can be understood in terms of the long wavelength of the barotropic tide and that it is accurately resolved with all grid resolutions used. When stratification was included it had a negligible effect upon surface elevation, although a baroclinic internal tide was produced. The spatial distribution of surface baroclinic tidal current ellipses showed that it was primarily generated along the shelf edge and in the region of the seamounts, with some propagation away from its generation region. A more detailed discussion of this with appropriate energy flux vectors and distributions is given in XD98. Comparison of time series of baroclinic tidal current profiles over two tidal cycles from west to east along a cross section through the Anton Dohrn Seamount, and from south to north along the 500 m depth contour
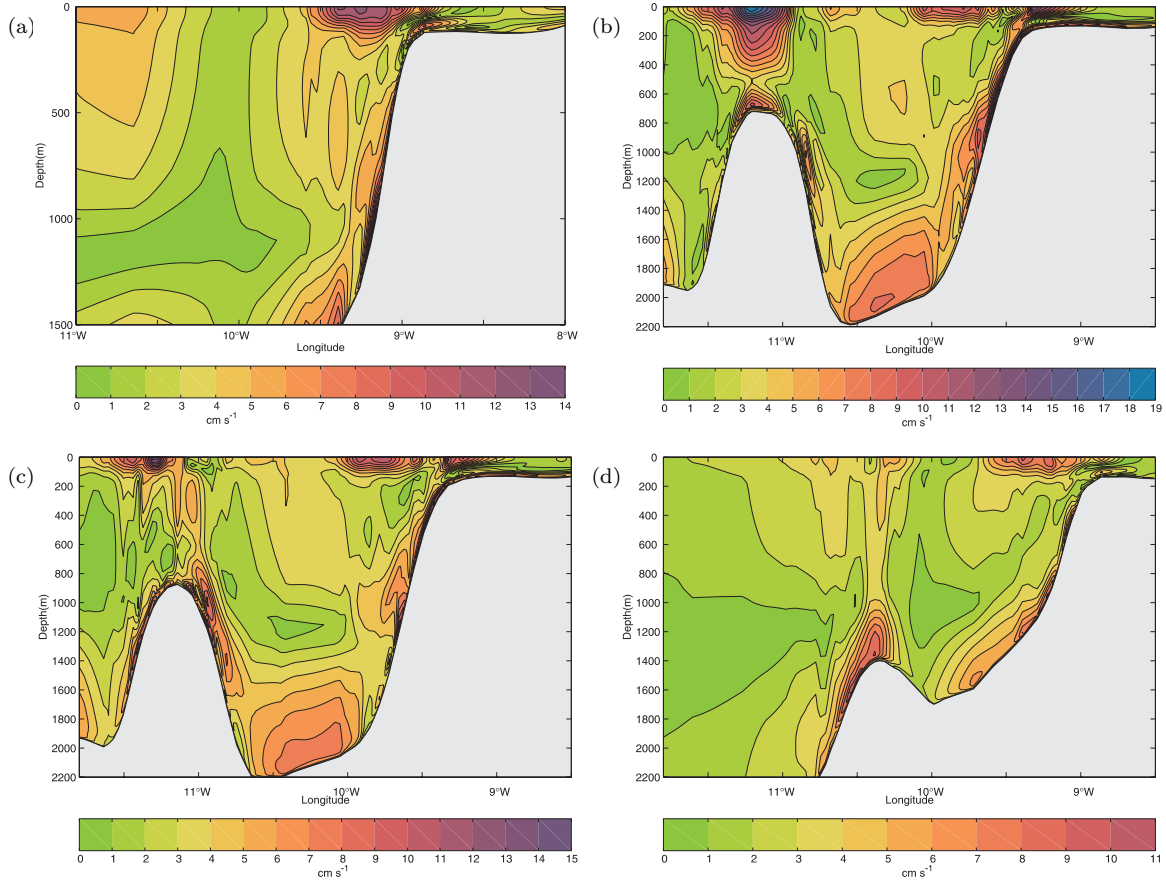
Fig. 10. As Fig. 9, but at cross sections a C2, b D1c, c D1s and d D2, with C=0.56.

showed significant spatial variability. At some locations differences between the coarse and fine grid solutions were evident. The differences between the solutions and that given by XD98 were quantified by comparison with current observations in the region.

To examine the effect of grid resolution in more detail, contours of u–current amplitude of the baroclinic tide were plotted along the same cross sections as in XD98. These showed that the coarse grid solution could not reproduce the surface intensification of the internal tide or the regions of local generation along shelf slopes. However, the surface intensification was reproduced with the finer grid model which showed regions of stronger intensification than those found by XD98. This suggests that the finer mesh finite element model is more accurate in generating and propagating the internal tide than the finite difference grid used in XD98. However, in some generation regions, along steep slopes there appeared to be some physically unrealistic small–scale waves in the finite element model that had to be removed by increasing the coefficient in the Smagorinsky formulation of horizontal eddy viscosity.

The intercomparison of the finite element model with two different horizontal grid resolutions and the finite difference model of XD98 presented here demonstrates a number of points. In particular, it shows that the finite element model can reproduce the internal tide off the west coast of Scot-

land, provided a sufficiently fine grid is used in the generation regions, and the adjacent sea regions into which the internal tide propagates. The ability to refine the mesh in regions where higher resolution is required is a major advantage over a regular grid. However, a rapid local refinement as shown by HD05 can affect internal wave propagation leading to increased energy at small scales that must be removed by an enhancement of a local scale–selective filter such as the Smagorinsky form of horizontal viscosity.

Acknowledgements

References

Blumberg, A. F., Mellor, G. L., 1987. A description of a three-dimensional coastal ocean circulation model. No. 4

in Coastal and Estuarine Sciences. American Geophysical Union, Washington, DC, p. 208pp.

Craig, P. D., 1987. Solutions for internal tide generation over coastal topography. Journal of Marine Research 45, 83–105.

Davies, A. M., Kwong, S. C. M., 2000. Tidal energy fluxes and dissipation on the European continental shelf. Journal of Geophysical Research 105, 21,969–21,989.

Davies, A. M., Xing, J., 2003. On the interaction between internal tides and wind induced near inertial currents at the shelf edge. Journal of Geophysical Research 108(C3), 3099, doi:10.1029/2002JC001375.

Hall, P., Davies, A. M., 2005. Effect of coastal boundary resolution and mixing upon internal wave generation and propagation in coastal regions. Ocean Dynamics 55, 248–271.

Huthnance, J. M., 1995. Circulation, exchange and water masses at the ocean margin: the role of physical processes at the shelf edge. Progress in Oceanography 35, 353–431.

Ip, J. T. C., Lynch, D. R., 1995. Comprehensive coastal circulation simulation using finite elements: nonlinear prognostic time-stepping model QUODDY3 users manual.

Johns, B., Dube, S. K., Mohanty, U. C., Sinha, P. C., 1981. Numerical simulation of the surge generated by the 1977 Andhra cyclone. Quarterly Journal of the Royal Meteorological Society 107, 919–934.

Lamb, K. G., 2004. Non-linear interaction among internal wave beams generated by tidal flow over supercritical topography. Geophysical Research Letters 31, L09313.

Legg, S., 2004a. Internal tides generated on a corrugated continental slope. part ii. along-slope barotropic forcing. Journal of Physical Oceanography 34, 1824–1838.

Legg, S., 2004b. Internal tides generated on a corrugated slope. part i: Cross-slope barotropic forcing. Journal of Physical Oceanography 34, 156–173.

Luettich Jr., R. A., Westerink, J. J., 1995. Continental shelf scale convergence studies with a barotropic tidal model. American Geophysical Union, Washington, DC, pp. 349–372.

Luyten, P. J., Carniel, S., Umgiesser, G., 2002. Validation of turbulence closure parameterizations for stably stratified flows using the PROVESS turbulence measurements in the North Sea. Journal of Sea Research 47, 239–267.

Luyten, P. J., Deleersnijder, E., Ozer, J., Ruddick, K. G., 1996. Presentation of a family of turbulence closure models for stratified shallow water flows and preliminary application to the Rhine outflow region. Continental Shelf Research 16, 101–130.

Lynch, D. R., Ip, J. T. C., Naimie, C. E., Werner, F. E., 1995. Convergence studies of tidally-rectified circulation on Georges Bank. American Geophysical Union, Washington, DC, pp. 154–174.

Lynch, D. R., Naimie, C. E., 1993. The M_2 tide and its residual on the outer banks of the Gulf of Maine. Journal of Physical Oceanography 23, 2222–2253.

New, A. L., 1988. Internal tidal mixing in the bay of biscay. Deep-Sea Research 35, 691–709.

Sherwin, T. J., 1988. Analysis of an internal tide observed on the Malin Shelf, north of Ireland. Journal of Physical Oceanography 18, 1035–1050.

Sherwin, T. J., Taylor, N. K., 1990. Numerical investigations of linear internal tide generation in the Rockall Trough. Deep-Sea Research 37, 1595–1618.

Smagorinsky, J., 1963. General circulation experiments with the primitive equations I. The basic experiment. Monthly Weather Review 91, 99–164.

Walters, R. A., 1987. A model for tides and currents in the English Channel and North Sea. Advances in Water Resources 10, 138–148.

Walters, R. A., 2005. Coastal ocean models: two useful finite element methods. Continental Shelf Research 25, 775–794.

Walters, R. A., Werner, F. E., 1989. A comparison of two finite element models of tidal hydrodynamics using a North Sea data set. Advances in Water Resources 12, 184–193.

Werner, F. E., 1995. A field test case for tidally forced flows: a review of the tidal flow forum. American Geophysical Union, Washington, DC, pp. 269–284.

Xing, J., Davies, A. M., 1997a. Application of a range of turbulence energy models to the computation of the internal tide. International Journal of Numerical Methods in Fluids 26, 1055–1084.

Xing, J., Davies, A. M., 1997b. Formulation of a three-dimensional shelf edge model and its application to internal tide generation. Continental Shelf Research 18, 405–440.

Xing, J., Davies, A. M., 1997c. The influence of wind effects upon internal tides in shelf edge regions. Journal of Physical Oceanography 27, 205–262.

Xing, J., Davies, A. M., 1998. A three-dimensional model of internal tides on the Malin-Hebrides shelf and shelf edge. Journal of Geophysical Research 103(C) (12), 27821–27847.

Xing, J., Davies, A. M., 1999. The influence of topographic features and density variations upon the internal tides in shelf edge regions. International Journal of Numerical Methods in Fluids 31, 535–577.

Xing, J., Davies, A. M., 2001a. Non-linear effects of internal tides on the generation of the tidal mean flow at the Hebrides shelf edge. Geophysical Research Letters 28, 3939–3942.

Xing, J., Davies, A. M., 2001b. A three-dimensional baroclinic model of the Irish Sea: Formation of the thermal fronts and associated circulation. Journal of Physical Oceanography 31, 94–114.